UNIVERSIDADE DE LISBOA
FACULDADE DE CIÊNCIAS
DEPARTAMENTO DE FÍSICA

MR-based pseudo-CT generation using water-fat decomposition and Gaussian mixture regression

Joaquim Manuel Faria Martins da Costa

Mestrado Integrado em Engenharia Biomédica e Biofísica
Perfil em Radiações em Diagnóstico e Terapia

Dissertação orientada por:
Prof. Dr. Peter Seevinck
Prof. Dr. Alexandre Andrade

2017

Resumo

O uso de tomografia computorizada (CT) é considerado como a prática clínica adequada para aplicações clínicas onde a simulação da atenuação de radiação pelos tecidos corporais é necessária, tais como a correcção de atenuação dos fotões em Tomografia de Emissão de Positrões (PET) e no cálculo da dosagem a ser administrada durante o planeamento de radioterapia (RTP).

Imagens de ressonância magnética (MRI) têm vindo a substituir o uso de TC em algumas aplicações, sobretudo devido ao seu superior contraste entre tecidos moles e ao facto de não usar radiação ionizante. Desta forma, técnicas como PET-MRI e o planeamento de radioterapia apenas com recurso a imagens de ressonância magnética são alvo de uma crescente atenção. No entanto, estas técnicas estão limitadas pelo facto de imagens de ressonância magnética não fornecerem informação acerca da atenuação e absorção de radiação pelos tecidos.

Normalmente, de forma a solucionar este problema, uma imagem de tomografia computorizada é adquirida de forma a realizar a correcção da atenuação dos fotões, assim como a dose a ser entregue em radioterapia. No entanto, esta prática introduz erros aquando do alinhamento entre as imagens de MRI e CT, que serão propagados durante todo o procedimento. Por outro lado, o uso de radiação ionizante e os custos adicionais e tempo de aquisição associado à obtenção de múltiplas modalidades de imagem limitam a aplicação clínica destas práticas.

Assim, o seguimento natural prende-se com a completa substituição do uso de CT por MRI. Desta forma, o desenvolvimento de um método para a obtenção de uma imagem equivalente a CT usando MRI é necessário, sendo a imagem resultante designada de pseudo-CT.

Vários métodos foram desenvolvidos de forma a construir pseudo-CT, usando métodos baseados na anatomia do paciente ou em métodos de regressão entre CT e MRI. No entanto, no primeiro caso, erros significativos são frequentes devido ao difícil alinhamento entre as imagens em casos em que a geometria do paciente é muito diferente da presente no atlas. No segundo caso, a ausência de sinal no osso cortical em MRI, torna-o indistinguível do ar. Sequências que usam um tempo de eco muito curto são normalmente utilizadas para distinguir osso cortical de ar. No entanto, para áreas com maior dimensão, como a área pélvica, dificuldades relacionadas com o equipamento e com o ruído limitam a sua aplicação nestas áreas. Por outro lado, estes métodos utilizam frequentemente diferentes imagens de MRI de forma a obter diferentes contrastes, aumentando assim o tempo de aquisição das imagens.

Nesta dissertação, é proposto um método para a obtenção de um pseudo-CT baseado na combinação de um algoritmo de decomposição de água e gordura e um modelo de regressão de mistura gaussiana para a região pélvica através da aquisição de sequências de MRI convencionais. Desta forma, a aquisição de diferentes contrastes é obtida por pós-processamento das imagens originais.

Desta forma, uma imagem ponderada em T_1 foi adquirida com 3 tempos de eco. Um algoritmo de decomposição do sinal de ressonância magnética em sinal proveniente de água e gordura foi utilizado, permitindo a obtenção de duas imagens, cada uma representando apenas o sinal da água e gordura, respectivamente. Usando estas duas imagens, uma imagem da fracção de gordura em cada *voxel* foi também calculada. Por outro lado, usando o primeiro e o terceiro eco foi possível calcular o decaimento de sinal devido a efeitos relacionados com o decaimento T_2*. O método para gerar o pseudo-CT baseia-

se num modelo de regressão duplo entre as variáveis relacionadas com MRI e CT. Assim, o primeiro modelo aplica-se aos tecidos moles, enquanto que o segundo modelo se aplica aos tecidos ósseos. A segmentação entre estes tecidos foi realizada através da delineação manual dos tecidos ósseos. No caso do modelo de regressão para os tecidos moles, o modelo consiste numa regressão polinomial entre as imagens da fracção de gordura e os valores de CT. A ordem do polinómio usada foi obtida pela minimização do erro absoluto médio. No caso do modelo de regressão para os tecidos ósseos, um modelo de regressão de mistura gaussiana foi aplicado usando as imagens de gordura, água, de fracção de gordura e de R_2*. Estas variáveis foram selecionadas, uma vez que estudos prévios correlacionam esta com a densidade mineral óssea, que por sua vez está relacionada com as intensidades em CT. A influência de incluir no modelo de regressão informação acerca da vizinhança foi estudada através da inclusão de imagens do desvio padrão nos 27 voxéis na vizinhança das variáveis previamente incluídas no modelo. O número de componentes a usar no modelo de regressão de mistura gaussiana foi obtido através da minimização do critério de Akaike. O pseudo-CT final foi obtido pela sobreposição das imagens obtidas através do duplo modelo de regressão, seguido da aplicação de um filtro gaussiano com desvio padrão de 0.5 de forma a mitigar os erros na segmentação dos tecidos ósseos. Este método foi validado usando imagens da zona pélvica de 6 pacientes usando um procedimento l*eave-one-out-cross-validation* (LOOCV). Durante este procedimento, o modelo foi estimado através das variáveis de 5 pacientes (imagens de treino) e aplicado às variáveis relacionadas com MRI do paciente restante (imagem de validação), de forma a gerar o pseudo-CT. Este procedimento foi repetido para todas as seis combinações de imagens de treino e de validação e os pseudo-CT obtidos foram comparados com a imagem TC correspondente.

No caso do modelo para os tecidos moles, verificou-se que a utilização de um polinómio de segundo grau permitia a obtenção de melhores resultados. Da mesma forma, verificou-se que a inclusão de informação acerca da vizinhança permitia uma melhor estimativa dos valores de pseudo-CT no caso dos tecidos ósseos. A segmentação dos tecidos ósseos foi considerada adequada uma vez que o valor médio do coeficiente de Dice entre estes tecidos e o osso em CT foi de 0.91 ±0.02. O valor médio do erro absoluto entre o pseudo-CT e a correspondente CT para todos os pacientes foi de 37.76±3.11 HU, enquanto que no caso dos tecidos ósseos o valor foi de 96.61±10.49 HU. Um erro médio de -2.68 ± 6.32 HU foi obtido, denotando a presença de *bias* no processo. Por outro lado, valores médios de *peak-to-signal-noise-ratio* (PSNR) e *strucutre similarity índex* (SSIM) de 23.92±1.62 dB e 0.91±0.01 foram obtidos, respectivamente. Os maiores erros foram encontrados no recto, uma vez que o ar não foi considerado neste método, nas interfaces entre diferentes tecidos, devido a erros no alinhamento das imagens, e nos tecidos ósseos.

Desta forma, o método de obtenção de um pseudo-CT proposto nesta dissertação demonstrou ter potencial para permitir uma correcta estimativa da intensidade em CT. Os resultados obtidos demonstram uma melhoria significativa quando comparados com outros métodos encontrados na literatura que se baseiam num método relacionado com a intensidade, enquanto que se encontram na mesma ordem de magnitude de métodos baseados na anatomia do paciente. Para além disso, quando comparados com os primeiros, este método tem a vantagem de apenas uma sequência MRI ser utilizada, levando a uma redução no tempo de aquisição e nos custos associados. Por outro lado, a principal limitação deste método prende-se com a segmentação manual dos tecidos ósseos, o que dificulta a sua implementação clínica. Desta forma, o desenvolvimento de técnicas de segmentação automáticas dos tecidos ósseos torna-se necessária, sendo exemplos destas técnicas a criação de um *shape model* ou através da segmentação baseada num atlas. A combinação destes métodos com o método descrito nesta dissertação pode permitir a obtenção de uma alternativa às imagens de CT para o cálculo das doses em radioterapia e correcção de atenuação em PET-MRI.

Palavras-Chave: Ressonância Magnética, Tomografia Computorizada, pseudo-CT, Decomposição de água e gordura, Regressão de mistura gaussiana

Abstract

Purpose: Methods for deriving computed tomography (CT) equivalent information from MRI are needed for attenuation correction in PET-MRI applications, as well as for dose planning in MRI based radiation therapy workflows, due to the lack of correlation between the MR signal and the electron density of different tissues. This dissertation presents a method to generate a pseudo-CT from MR images acquired with a conventional MR pulse sequence.

Methods: A T_1-weighted Fast Field Echo sequence with 3 echo times was used. A 3-point water-fat decomposition algorithm was applied to the original MR images to obtain water and fat-only images as well as a quantitative fat fraction image. A R_2* image was calculated using a mono-exponential fit between the first and third echo of the original MR images. The method for generating the pseudo-CT includes a dual-model regression between the MR features and a matched CT image. The first model was applied to soft tissues, while the second-model was applied to the bone anatomy that were previously segmented. The soft-tissue regression model consists of a second-order polynomial regression between the fat fraction values in soft tissue and the HU values in the CT image, while the bone regression model consists of a Gaussian mixture regression including the water, fat, fat fraction and R_2* values in bone tissues. Neighbourhood information was also included in the bone regression model by calculating an image of the standard deviation of 27-neighbourhood of each voxel in each MR related feature. The final pseudo-CT was generated by combining the pseudo-CTs from both models followed by the application of a Gaussian filter for additional smoothing. This method was validated using datasets covering the pelvic area of six patients and applying a leave-one-out-cross-validation (LOOCV) procedure. During LOOCV, the model was estimated from the MR related features and the CT data of 5 patients (training set) and applied to the MR features of the remaining patient (validation set) to generate a pseudo-CT image. This procedure was repeated for the all six training and validation data combinations and the pseudo-CTs were compared to the corresponding CT image.

Results: The average mean absolute error for the HU values in the body for all patients was 37.76±3.11 HU, while the average mean absolute error in the bone anatomy was 96.61±10.49 HU. No large differences in method accuracy were noted for the different patients, except for the air in the rectum which was classified as soft tissue. The largest errors were found in the rectum and in the interfaces between different tissue types.

Conclusions: The pseudo-CT generation method here proposed has the potential to provide an accurate estimation of HU values. The results here reported are substantially better than other voxel-based methods proposed. However, they are in the same range as the results presented in anatomy-based methods. Further investigation in automatic MRI bone segmentation methods is necessary to allow the automatic application of this method into clinical practice. The combination of these automatic bone segmentation methods with the model here reported is expected to provide an alternative to CT images for dose planning in radiotherapy and attenuation correction in PET-MRI.

Keywords: Magnetic Resonance, Computed Tomography, pseudo-CT, water-fat decomposition, Gaussian mixture regression

Acknowledgments

Firstly, I would like to start by thanking my supervisor **Peter Seevinck** from the University Medical Center (UMC) Utrecht, who gave me the opportunity to join his research group to perform this amazing project. During this internship, he was a great motivator, patient and he was always available to teach me everything that I wanted to know and basically for all the guidance during my stay at UMC Utrecht. I learned a lot because of him and he was not just a good supervisor but also a great friend. I have nothing more than absolute respect and admiration for him and I wish him all the best in the world. I also want to thank **Marijn van Stralen** who was essential for my work for always being there to help me and advise me. His expertise, understanding and patience added considerably to my project and I have the most respect for him and his work and dedication.

I would also like to thank **Matteo Maspero** and **Frank Zijlstra** for all the support and great advises that were essential for a better understanding of this project. Furthermore, a big thanks to Harry Hu, Chen Cui and Joshua Kim for being available to clarify my doubts about their methods throughout the project.

A big thank you to everybody in the Image Science Institute from UMC who received me so well and who made me feel that I was at home every day. A special thanks to **Valerio Manippa** and **Luis Alberto** for being my office buddies, for their friendship and for the great moments and happy times.

I would also like to thank to my supervisor **Alexandre Andrade**, for all the support and for being always available to help me regarding the problem! I must also acknowledge the Reitoria da Universidade de Lisboa for the financial support, under the ERASMUS program, that made this internship possible.

In addition, a very special thantks to all the people I met in Utrecht, especially **Richard Heery**, **Hugo Suberbie**, **Adrien Damseaux** and **Samuel Bradley** for the wonderful adventures we had. Also, all the people from the **Bilstraat family** and the **UCU guys**, you'll never be forgotten.

To all my friends in Portugal, from Lisbon to Guimarães, from FCUL, to RUEM, passing by Anexo and finishing in the Arco guys, I could not thank you enough for what you've done for me!

Last but not least, there are no words to describe how grateful I am to my wonderful parents **Joaquim** and **Maria** for all the support and for making the person that I am, to my sister and nephew **Marisa** and **Andre**. A big and special thanks to my brother **Miguel** for all the support and for being always an example and a tutor for me!

List of Acronyms

2D – Two dimensional

3D – Three dimensional

AIC – Akaike's Information Criterium

CT – Computed Tomography

dB - Decibel

dUTE – Differential Ultrashort Echo Time

EM – Expectation Maximization

FF – Fat Fraction

FFE – Fast Field Echo

FID – Free Inductive Decay

FOV – Field of View

GE – Gradient Echo

GMM – Gaussian Mixture Model

GMR – Gaussian Mixture Regression

HU – Hounsfield Unit

IDEAL – Iterative Decomposition of Water and Fat with Echo Asymmetry and Least Squares Estimation

IP – In Phase

ISI – Image Sciences Institute

LOOCV – Leave-One-Out-Cross-Validation

MAE – Mean Absolute Error

ME – Mean Error

mm- millimetre

MR – Magnetic Resonance

MRI – Magnetic Resonance Imaging

ms – millisecond

MSE – Mean Square Error

NMR – Nuclear Magnetic Resonance

NSA – Number of Samples Average

NSSD – Local Sum of Squared Differences

OP – Out of Phase

PD – Proton Density

PET – Positron Emission Tomography

PSNR – Peak Signal-to-Noise Ratio

QSM – Quantitative Susceptibility Mapping

RF - Radiofrequency

ROI – Region of Interest

RTP – Radiotherapy Planning

SE – Spin Echo

SNR – Signal-to-Noise Ratio

SSIM – Structure Similarity Index

STIR – Short-Tau Inversion Recovery

T - Tesla

TE – Echo Time

TR - Repetition Time

UMC – University Medical Centre

UTE – Ultrashort Echo Time

List of Figures

Contents

Chapter 1

Introduction

Computed tomography (CT), with its high availability and geometric accuracy, has proven to be an invaluable tool for many clinical applications where radiation transport simulation is necessary. Since the voxel's intensity of a CT image is related to the tissue electron density, CT images may be used to quantify the attenuation of X-rays within a tissue, which, in turn, is necessary to simulate radiation transport. For this reason, CT is considered as the golden standard technique of both radiotherapy planning (RTP) and attenuation correction of Positron Emission Tomography (PET) images [1] [2].

Despite the many advantages of CT, Magnetic Resonance Imaging (MRI) is starting to replace the use of CT in some applications, mainly due to improved soft tissue contrast and the lack of ionizing radiation.

PET-MRI is an emerging technology with enormous potential for improvements over PET-CT for staging, multiparametric therapy planning and functional assessment of treatment response. PET-MRI was shown to outperform PET-CT in the diagnostic and evaluation of some lesions and diseases, such as breast cancer, prostate cancer and the detection of soft tissue lesions in the brain, liver and lymph nodes [3] [4] [5]. However, current PET-MRI systems lack accurate attenuation correction, which is the most significant of all the corrections applied during PET image reconstruction[6] [7] [8] [9]. Since the MRI voxel's intensity is governed by the proton density and relaxation effects, there is no relation between the MRI voxel's intensity and the tissue electron density, necessary to perform the attenuation correction[10].

MR-based RTP and integrated MRI treatment machines, such as MRI linear accelerator combinations, are another emerging technologies, with the potential to improve tumour visualization during treatment compared to conventional systems that use ionizing radiation[11] [12] [13]. Several studies have shown the superiority of MRI for contouring tumour and organs at risk volumes in terms of target volume delineation[14] [15] [16]. However, similar to the attenuation correction for PET-MRI, radiation absorption in tissue depends on photon interaction with electrons, and MRI does not directly relate to such effects.

Traditionally, to overcome these problems, CT is also performed in order to calculate the attenuation correction map as well as the dose to be delivered. However, this practice introduces systematic errors in MRI-CT registration, that will cause ambiguities in the following PET-MRI and MR-RTP procedures. Furthermore, the use of ionizing radiation and the additional costs and scanning time associated with obtaining and using multiple imaging modalities are serious limitations of this practice[17].

Thus, the natural follow-up is to completely replace the use of CT by MRI. When residing to MRI-only techniques, there must be an accurate method to derive CT equivalent data from the MR data to be able to perform attenuation correction and dose calculations in the same way as it is done when using a real CT image. MRI-based CT-equivalent images are generally called pseudo-CT images (or synthetic CT or substitute CT). This approach brings many benefits including the reduction of imaging

acquisition costs and radiation exposure, as well as the elimination of the registrations errors between different imaging modalities[18].

Several methods were developed in order to generate a pseudo-CT, either by using an anatomy-based approach or a voxel-based approach. The main challenge for the first case lies in the difficulty of accurate registration when the patient's geometry is very different from the atlas, which will lead to significant errors. When using a voxel-based approach, one of the main problems is the lack of signal in cortical bone, making it indistinguishable from the air[18]. Ultrashort Echo Time (UTE) sequences have been proposed to distinguish bone and air[19]. However, for areas with a large field of view (FOV), such as the pelvic area, difficulties related to the hardware and noise considerations associated with UTE sequences make them unsuitable for clinical application[20]. Furthermore, most of these methods also acquire different MR sequences in order to obtain different contrasts to generate the pseudo-CT, which leads to an increase in scanning time[21] [22] [23].

In this dissertation, we propose to develop a MRI conversion approach for the generation of pseudo-CTs using a combination of an MR-based water-fat decomposition algorithm with a Gaussian mixture regression algorithm for the pelvic area. In this way, the acquisition of different sequences to obtain different contrasts will be replaced by contrasts that could be obtained through post-processing of images from a single acquisition. Specifically, water and fat images may be obtained from a water-fat-decomposition algorithm. Moreover, other semi-quantitative images may be obtained by the conjugation of these two images, such as a fat fraction image, that may provide a different contrast between voxels. Furthermore, as a gradient-echo sequence is used, an estimation of the T_2* decay is possible. In this work, a dual-model regression is applied, with one model applied to soft tissue and the second model tuned to the bone anatomy obtained by segmentation. As soft tissues are mainly constituted by water and fat, the use of a water-fat decomposition scheme seems obvious for the separation of these two species in the MR images, followed by HU values assignment through regression. Regarding the bone anatomy, it was demonstrated the correlation of the T_2* decay as well as proportion of the fat signal in a voxel with the bone mineral density [17][24] [25] [26] [27]. Furthermore, the correlation between the HU values and the bone mineral density was also demonstrated, with higher bone mineral density tissues, normally caused by the presence of minerals such as calcium, representing denser bones [28]. By including the water and fat information together with information about the T_2* decay in a Gaussian mixture regression procedure, it is expected to obtain a good estimation of the HU units in the bone anatomy. Also, the influence of including neighbourhood information for HU estimating in the bone anatomy is investigated. This approach was evaluated on six patient datasets for which CT and MR images were available for prostate sites, by using a leave-one-out-cross-validation procedure. The pseudo-CTs were obtained for the six patients and were compared to the corresponding CT images.

The goal of this project was to investigate if the conversion of MR-data into CT equivalent data could be established without prior CT information and by a better fundamental understanding of the MR signal itself, aiming at completely removing CT acquisitions of the traditional workflow of PET-MRI and MR-RTP.

This dissertation describes the work performed at Image Sciences Institute (ISI), part of the University Medical Center (UMC) of Utrecht, The Netherlands, during a 10 months internship. The work is here organized in 5 chapters. Chapter 2 provides background information about CT imaging, MR imaging and MR-based water-fat decomposition, different approaches to derive a pseudo-CT and Gaussian mixture regression. Chapter 3 describes the data, software and methods used in this work.

Chapter 4 presents the relevant results and also the discussion. Finally, Chapter 5 summarizes the main conclusions and possible future work.

Chapter 2

Background

2.1. CT imaging

In CT, transaxial X-ray projections are computed to create cross-sectional images of the human body. In a CT scanner, the X-ray tube rotates around the body, while the beams pass through the patient at different angles. The intensity of the attenuated beams is measured and then converted into an electric signal using detectors placed on the opposite side of the X-ray tube. After processing, these signals are transformed into attenuation values consisting of the CT raw data[29]. This data is then converted into an image using one of several possible a CT reconstruction algorithms, of which the filtered back-projection algorithm is the most widely used[30]. As a final result, each voxel of the reconstructed CT image represents a scanned voxel with a specific Hounsfield Unit (HU), describing the degree of attenuation relative to water[31]:

$$HU(i,j) = 1000 \times \frac{\mu(i,j) - \mu_w}{\mu_w} \tag{2.1}$$

where $\mu(i,j)$ represents the linear attenuation coefficient of the voxel (i, j) and μ_w is the linear attenuation coefficient for water at the same spectrum of photon energies.

The HU is a measure that describes the absorption properties of the tissue relative to water. Therefore, different HU values are responsible for creating different contrasts in a CT image, as it can be seen in figure 2.1[31]. Generally, bone appears brighter since it has the highest HU values (ranging from 400 to 1800 HU), air is black as it presents the smallest HU values (-1000 HU), while soft tissues present different shades of grey according to their HU values[32] [33]. The similarity in HU values for different soft tissues makes the distinction between tumours and healthy tissues difficult.

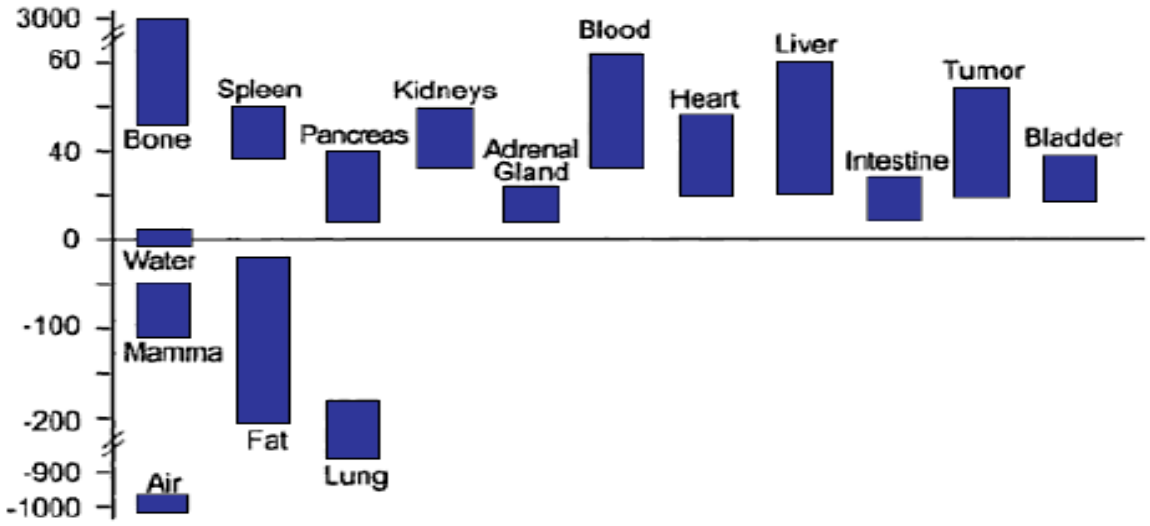

Figure 2.1 - HU values for different tissue types in human body. y-scale represents the HU scale [33].

The accuracy of attenuation correction and dose calculations based on CT images is determined by the precision of HUs to relative electron densities conversion. This relationship is called calibration curve[34].

2.2. MR Imaging

2.2.1. Physical Principles

Due to the magnetic properties of the atomic nuclei, protons and neutrons present a spin angular momentum and an associated magnetic moment $\vec{\mu}$. In Nuclear Magnetic Resonance (NMR), instead of a single particle, it is important to study all particles[35]. Thus, it is important to convert from the magnetic momentum of a single particle to a measure that represents the sum of all magnetic momenta. This sum can be represented by a vector called magnetization, $\vec{M}$:

$$\vec{M} = \sum \vec{\mu_i} \tag{2.2}$$

For NMR's studies, two components of $\vec{M}$ are important: $\overrightarrow{M_{xy}}$, the transverse magnetization, and $\overrightarrow{M_z}$, the longitudinal magnetization. In a state without any external force applied, the magnetic momentum of each particle is random, and therefore $\vec{M}$ is equal to 0, as it can be seen in figure 2.2[35] [36].

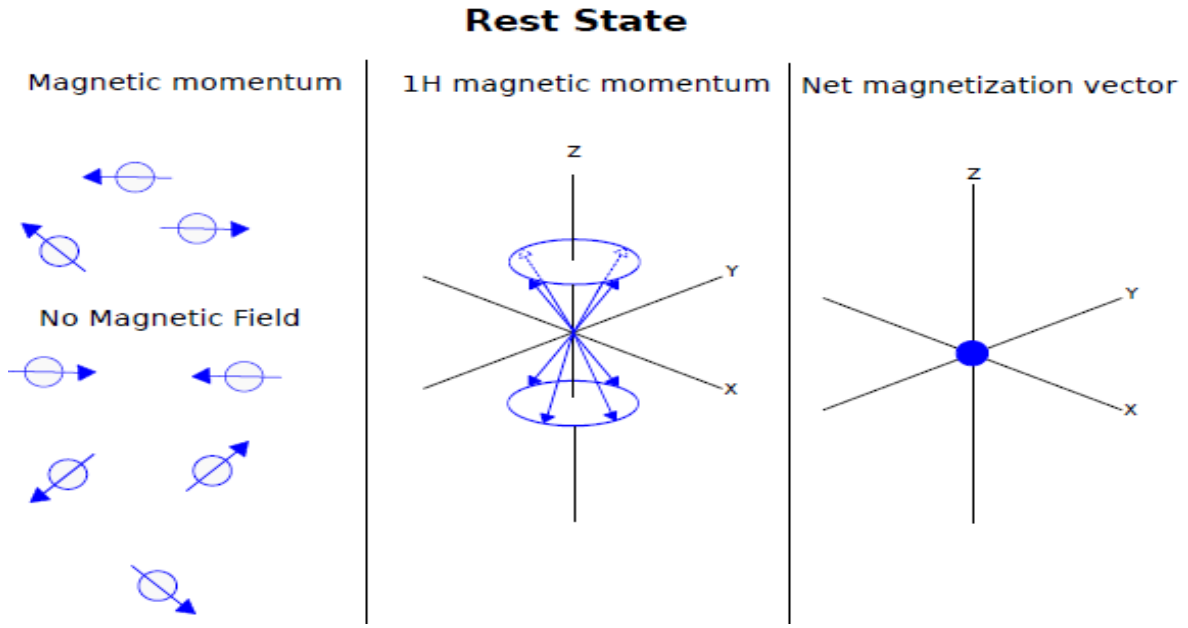

Figure 2.2 – Illustration of a single particle momentum and resulting magnetization vector when there is no external force applied [36].

When an external magnetic field B_0 is applied (normally in z-component), the magnetic momentum of each particle will align with the direction of B_0, and therefore the magnetization vector in the z-direction is not 0, as represented in figure 2.3. For ^1H, which is the most typical isotope used in NMR, only two magnetic momenta are allowed (±1/2) and therefore two energy states are allowed, having the same energy. However, if the proton is placed into B_0, the angular momentum will align with

the field direction, making that the resultant magnetic momentum does not have the same energy for both states. The state with the z-component parallel to B_0 presents a lower energy than the state with the z-component anti-parallel. In this way, there are more particles align parallel to B_0 than anti-parallel and $\vec{M}$ will be parallel to B_0 [36][37].

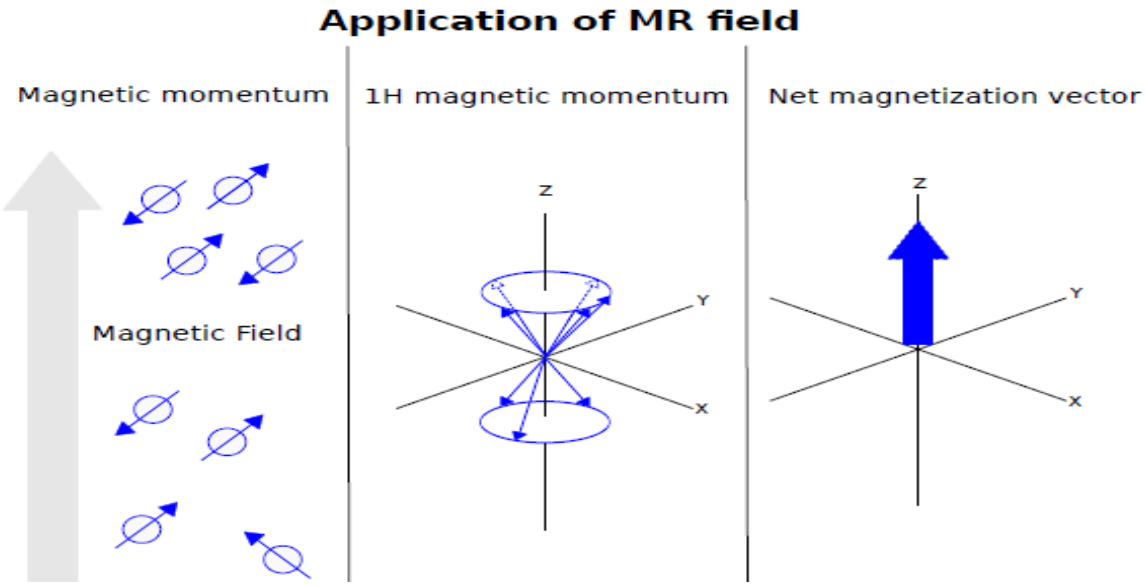

Figure 2.3 – Illustration of a single particle momentum and resulting magnetization vector when there B_0 magnetic field is applied [36].

It is possible that spin transition from one state to the other one happens by supplying energy to the system. This energy has to be equal to the difference of energy of both states. This energy supplying can be done by applying a radio frequency (RF) pulse with frequency equals to

$$\omega_0 = \gamma B_0 \tag{2.3}$$

Where ω_0 is named Larmor frequency and γ is the gyromagnetic ratio, that is specific to the used isotope (for ^{1}H, $\gamma/2\pi$=43 MHz/T).

When the RF pulse (B_1 field) is applied in the xy-plane with the Larmor frequency, the particles in the spin-up state can, therefore, transit to the spin-down state. Adding to this effect, the individual particles will rotate (precession movement) in phase (phase coherence) allowing a transverse magnetization to appear, as represented in figure 2.4. Regarding $\vec{M}$, the RF pulse will lead the rotation of this vector, and the angle of rotation (flip angle, α) will only depend on the amplitude of the B_1 field and the duration of the pulse (t):

$$\alpha = \gamma B_1 t \tag{2.4}$$

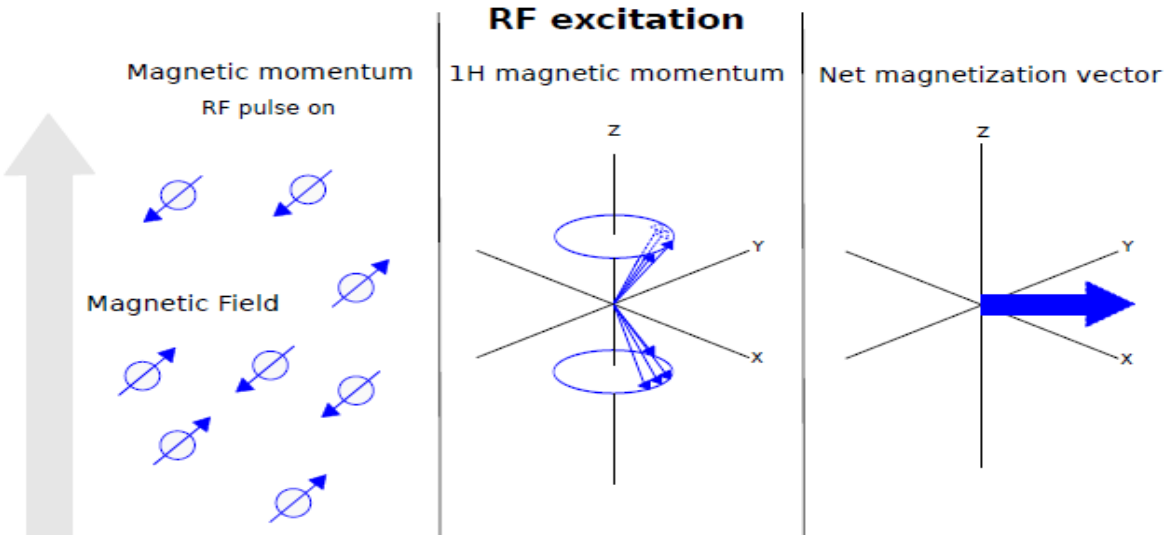

Figure 2.4 – Illustration of a single particle momentum and resulting magnetization vector when the RF-pulse (B_1 field) is applied [36].

As the RF pulse is stopped, the particles return to the rest state as well as $\vec{M}$. For this to happen, the particles emit a RF wave with the Larmor frequency, called the free inductive decay (FID). The return to the equilibrium state is called relaxation and is governed by two physical phenomena: spin-lattice relaxation and spin-spin relaxation[36][37] [38].

As the spins return to the spin-up state, $\overrightarrow{M_z}$ returns to the rest state (spin-lattice relaxation) due to energy dissipation to the spins' surroundings. This process is called T_1 recovery, described by

$$M_Z = M_0 \left(1 - e^{-t/T1}\right) \tag{2.5}$$

Where M_0 is the magnetization at t=0, and T_1 is the spin-lattice relaxation time or longitudinal time.

Moreover, after stimulation, the net magnetization starts to dephase (spin-spin relaxation), due to the inhomogeneities of B_0 and the interaction between the spins. This process is called T_2 decay and it is described by

$$M_{xy} = M_{xy0}\, e^{-t/T2} \tag{2.6}$$

Where T_2 is the spin-spin relaxation time or transverse relaxation time.

Although relaxation is the result of stochastic processes, some deterministic conditions, such as the inhomogeneity of B_0, causes different spins to precess with different resonance frequencies. The B_0 inhomogeneities may be caused by the presence of mineral such as iron and calcium, that create distortion in B_0[37]. Thus, the spins will dephase, causing the decay of the total transversal magnetization. In this way, the effective transversal relaxation time will be referred as T_2* and it is defined as

$$\frac{1}{T_2^*} = \frac{1}{T_2} + \frac{1}{T_2'} \tag{2.7}$$

Where T_2 is the stochastic contribution and T_2' the deterministic. By definition, T_2^* is always shorter than T_2.

T_1, T_2 and T_2^* relaxation times are dependent on the material composition and consequently also the acquired NMR signal.

However, as the FID signal quickly vanishes due to the T_2^* decay, it is difficult to acquire. Therefore, MRI pulse sequences are used for rephasing the spins. The coherent signal that is emitted after rephasing is designed by echo. In practice, the pulse sequences are always repeated with a fixed repetition time (TR) in order to reduce the noise and to achieve different space encoding in the different repetitions. There are two fundamental types of MR pulse sequences: Spin Echo (SE) and Gradient Echo (GE) sequences[37]. The remaining developed MR sequences derive in some way from the combination of the SE and GE sequences.

In a SE sequence, after applying a 90° RF-pulse, the transversal magnetization will decay exponentially according to T_2^*, due to differences in the frequency precession of different spins. If a second RF-pulse with a flip angle of 180° is applied, all spins will rotate 180° around the direction of the B_1 field, causing the inversion of the relative phases of the spins in the transversal plane, while the longitudinal magnetization continues unchanged. In this way, faster spins that were leading in-phase will now be lagging in phase. After the 180° pulse, these spins will catch up with the slower spins, causing the rephasing of the spins. This rephasing results in an echo signal. The time between the 90° pulse and the emission of the echo is called echo time (TE) [37].

Gradient echo sequences are created using a magnetic field gradient instead of a RF-pulse. After the excitation pulse, typically smaller than 90°, a gradient is switched on, causing the dephasing of the spins. Then, the polarity of the gradient is reversed, causing the spins' rephasing and the formation of an echo. As the spins' rephasing occurs only with respect to the gradient, and not to other sources of dephasing, the signal amplitude is dependent on the T_2^* decay[37].

This T_2^* decay can be quantified in GE sequences using:

$$\frac{1}{T_2^*} = R_2^* = -\frac{\log S(TE_n) - \log S(TE_1)}{TE_n - TE_1} \tag{2.8}$$

where $S(TE_n)$ is the signal intensity when the TE was equal to the n^{th} echo of the acquisition, TE_n is the echo time of the n^{th} echo of the acquisition. $S(TE_1)$ is the signal intensity of the first echo of the acquisition acquired at TE_1.

In this way, MR intensities can be correlated with proton densities, which are related to the number of hydrogen atoms in a volume, and tissue relaxation properties rather than with the attenuation properties of the tissues such as in CT. The density and relaxation time of protons in different tissues is used to create the required contrast and signal intensity for diagnostic purpose in MR images by changes in TE and TR. The contrasts are created based on a linear look up table, where magnitudes of the measured signals are converted to a grey tone.

Thus, there are 3 different types of contrasts in MR images that can be created by changing TE and TR: T_2-weighted images, T_1- weighted images and proton-density (PD) weighted images[39]. In T_2-weighted images, the TR and TE are both long and tissues with long T2, such as fluids, present the highest signal intensities, producing a bright appearance. T_2 images are often called as "pathology images" as the abnormal fluids appear bright against the dark normal tissue. In T_1-weighted images, long T_1 tissues give the weakest signal and appear dark, as fluids, and bright pixels are associated with

short T_1 values, such as fat based tissues. This contrast can be achieved by using short TR and TE. T_1 images are often called anatomy scans as they display clearly the boundaries between different tissues. PD-weighted images give a quantitative summary of the number of protons per unit tissue. The higher the number of protons in a tissue, the brighter the tissue will appear on the image. This contrast can be achieved by using a long TR and a short TE[39].

As for CT, MRI generates cross-sectional images of the human body. The RF pulse is therefore delivered only to the slice that is needed to be imaged. Slice position will be selected according to the central frequency of the applied RF pulse. After selecting slice thickness and position, the spatial position of the MR signal needs to be identified which is accomplished using spatial encoding. Spatial encoding comprises two steps, phase encoding and frequency encoding, requiring the application of additional gradients that will change the magnetic field strength along the x and y axis enabling unique spatial identification of each voxel. The raw-data space which is used to store the digitized MR signals during acquisition is called k-space. The k-space has two axes with the horizontal axis (k_x) representing the frequency information and the vertical axis (k_y) the phase information. The final MR image will be created from the raw data by applying the 2D- Fourier Transformation to the k-space after the scan is over[39].

2.2.2. Fat and water Magnetic Resonance Imaging

Most clinical magnetic resonance imaging applications detect the signal from protons, which compromise over 90% of nuclei in the human body. The detected protons are either part of water, bound to molecules or carbohydrates, or fat. Their respective signal intensities in imaging voxels results from a combination of their spin density, longitudinal and transverse relaxation times (T_1 and T_2, respectively), and the parameters of the imaging sequence used. By exploiting the particular characteristics of hydrogen, MRI can provide excellent contrast between soft tissue, according to whether they are bound to water or lipid molecules[40].

With its relatively short T_1 relaxation time, fat signal often appears bright in many important clinical imaging sequences and can obscure underlying pathology such as edema, inflammation, or enhancing tumours. For this reason, water-fat decomposition methods are necessary to supress or detect fat signal and improve visualization of these abnormalities[40].

Several techniques of water-fat decomposition were proposed such as the chemical shift saturation pulse and the short-tau inversion recovery (STIR). In the first technique, a frequency selective RF pulse and a spoiler gradient pulse are used in conjunction to first excite and then saturate the fat magnetization before water is excited during imaging[41]. In STIR, the longitudinal magnetization of fat is first flipped 180° by an inversion pulse and then allowed to relax back to its equilibrium along the magnetic field direction. Water magnetization, which is usually also flipped 180° by the same inversion pulse, is excited when the longitudinal magnetization of fat crosses the null point. Due to the short T_1 relaxation time of fat, water has usually relaxed only partially along the longitudinal axis at the time of excitation[42] [43].

Although the previous techniques can obtain a reliable fat suppression, for pseudo-CT generation purposes, detection rather than suppression is more valuable, once quantification of water and fat is necessary, since they present different HU values, as it can be seen in figure 2.1. Also, it was demonstrated that the quantitative fat fraction is correlated with bone mineral density, which is correlated with the HU values of bone[26] [28].

In this way, methods that could quantify the signal of water and fat are preferred over suppression techniques. These methods that are able to perform separation as well as quantification are referred as chemical shift water-fat decomposition techniques[40] [44].

2.2.2.1. Physics of water-fat imaging

2.2.2.1.1. NMR Spectrum of water and fat

The electronic shielding of the protons in fat molecules is greater than that experienced by protons in water molecules, resulting in different microscopic magnetic fields, and subsequently different proton resonance frequencies. Fat has a complex spectrum with multiple peaks, the largest of which is shifted downfield by ≈ 3.5 ppm from the water peak[40] [45].

The resulting chemical shift, Δf_{cs} in the resonance frequency is linearly related to the magnetic field strength B_0:

$$\Delta f_{cs} = \frac{\gamma}{2\pi} B_0 \times \Delta\delta\ [ppm] \times 10^{-6} \tag{2.9}$$

As the chemical shift is directly proportional to B_0, the chemical shift at 1.5 T is -210 Hz (fat precesses slower than water), while at 3 T, it doubles to -420 Hz at body temperature (37°C), as represented in figure 2.5[46].

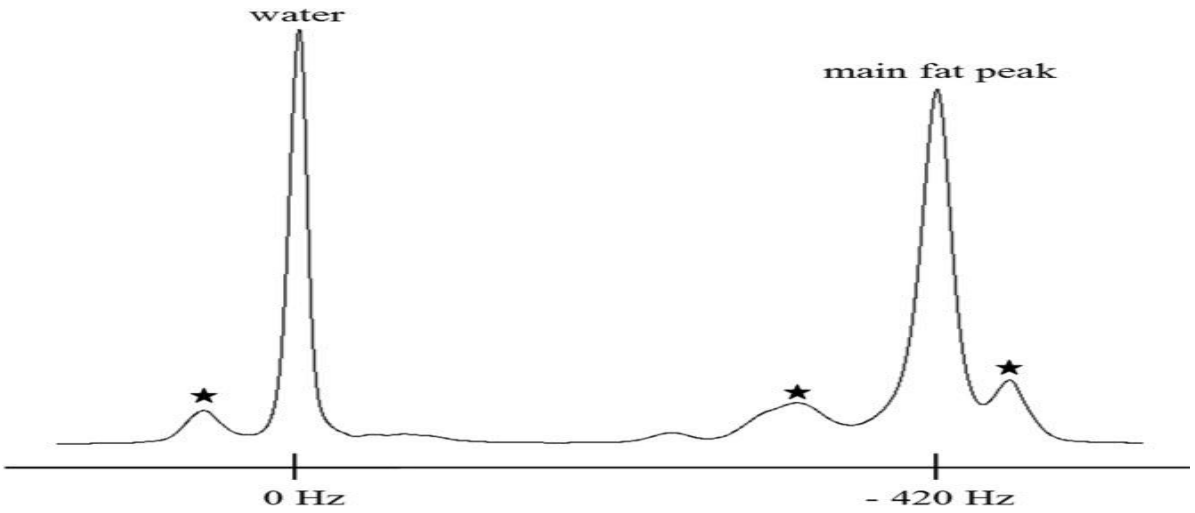

Figure 2.5 – Illustration of the resonance spectrum of water and fat at 3 Tesla. The stars represent the additional peaks of fat [40].

2.2.2.1.2. B_0 Inhomogeneities

Most of the water-fat separation techniques rely on the assumption that there are constant frequencies for fat and water across the image. However, in practical applications many factors can create inhomogeneities in the B_0 field that violate this assumption and result in imperfection suppression of fat[40].

Although the main magnet itself may have an imperfect magnetic homogeneity, this is a minor effect since modern MR scanners are shimmed to homogeneity within 1 ppm across the field of view (FOV). Magnetic susceptibility introduced by the patient leads to more significative B_0 inhomogeneities and it can be caused by several sources, such as air/tissue interfaces, ears or the bowel gas. These B_0

inhomogeneities have three main effects: distortion in the readout gradient, accelerated T_2* decay for gradient echo imaging and failed fat suppression which is the most relevant for the context of this work[40].

2.2.2.2. Water-Fat Separation Techniques

2.2.2.2.1. Chemical shift based water-fat separation

Chemical shift based water-fat separation methods comprise a class of approaches commonly known as "Dixon" water-fat separation. As for the frequency selective approach, the Dixon techniques rely on the water-fat chemical shift difference. However, the Dixon techniques encode the chemical shift difference into the signal difference with a modified data acquisition and then achieve the water/fat separation through post-processing. In its original approach, Dixon acquired an image with water and fat signal in-phase and another image with the signal 180° out-of-phase[44] [47]. The choice of the echo times to achieve these two images is done using

$$TE = \frac{\theta}{2\pi\,\Delta f_{cs}} \tag{2.10}$$

where θ is the phase shift between water and fat signal. In this way, the Dixon technique can be described by the following equation system:

$$\begin{cases} IP = W + F \\ OP = W - F \end{cases} <=> \begin{cases} W = \dfrac{(IP + OP)}{2} \\ F = \dfrac{(IP - OP)}{2} \end{cases} \tag{2.11}$$

where IP represents the in-phase image, OP the out-of-phase image, F the fat image and W the water image. As this approach only requires two images, it is considered a "two-point" method.

Unfortunately, Dixon's original approach was sensitive to B_0 inhomogeneities that resulted in water-fat swapping in the image[40]. Thus, this approach was subsequently modified to include a third image that was used to compensate for B_0 inhomogeneities. This three-point method acquire images at TE values that generate phase shifts of 0, +π and -π between the water and fat[48]. The additional information can be used to calculate a B_0 field inhomogeneity map (field map). By using phase unwrapping algorithms, this approach is able to remove the effects of field distortions, thereby avoiding water-fat swapping, turning this method more robust[44] [49] [50]. However, this technique increases the scan time and doesn't allow flexibility in the sequence design since the images have to be acquired at specific TE values[40].

To allow more flexibility in the pulse sequence design and, consequently, reduce the scan time, several methods were developed that allow arbitrary TE values to accomplishing the water-fat separation, such as the iterative decomposition of water and fat with echo asymmetry and least squares estimation (IDEAL)[51]. This method uses images acquired at arbitrary TE values together with an iterative least square estimation of the field map to accomplish a voxel-independent water-fat separation. However, in areas with severe field inhomogeneities this method still fails to obtain an accurate field map since, with this technique, the field map can be directly estimated only if the true field map ranges between ± $\Delta f_{cs}/2$. In practice, the field inhomogeneity may exceed this range[52]. Furthermore, these techniques normally use an alternating bipolar readout gradient to achieve scan efficiency and reduce

the echo spacing. The use of this alternating bipolar gradient turns the estimation of the field map susceptible to eddy-currents, which manifest itself as phase errors[53] [54] [55].

More recently, a water-fat separation method that uses a graph-cut algorithm to jointly estimate water/fat images and the field map was proposed[56]. In this approach, the estimation of the field map at all voxels is formulated as the minimization of a global criterion, which is the linear combination of the sum of the voxel-independent criteria and a field map smoothing penalty, and solve it using an iterative graph cut algorithm. This algorithm is further explained below.

2.2.2.2.1.1. Graph Cut Water-Fat decomposition algorithm

The graph cut water-fat estimation algorithm uses a multi-echo water and fat decomposition scheme, where a sequence of images is collected with different echo time shifts, t_1, t_2, t_n. The signal at each individual voxel is described by the following model[51] [56]:

$$s(r,t_n) = \left(\rho_{water}(r) + \rho_{fat}(r)e^{j2\pi\Delta f_{cs}t_n}\right)e^{-\varphi(r)t_n}, \quad n = 1, \dots, N \tag{2.12}$$

where $\rho_{water}(r)$ and $\rho_{fat}(r)$ are complex-valued concentrations of water and fat, respectively. The field map, f(r), is consolidated in $\varphi(r)$ through

$$\varphi(r) = [j2\pi\, \mathrm{f}(r)] \tag{2.13}$$

From this signal model, it is possible to observe that there are 2 complex unknows, $\rho_{water}(r)$ and $\rho_{fat}(r)$, and 1 real unknown, f(r), in a total of 5 (each complex unknown has a real and imaginary unknown). As each image contributes with a real and imaginary measurement, constituting two measurements per TE value, at least 3 images at different TE values have to be acquired, since the number of measurements has to be always equal or higher than the number of unknown parameters.

Also, in this signal model, it is assumed that fat only presents a single resonance frequency. However, fat has several peaks. In particular, the spectral peak from olefinic proton (5.3 ppm) is close to the water resonance frequency, which can cause some water-fat swapping[57]. One possible solution is to include in the signal model a weighted sum of the amplitudes of the fat peaks, by changing equation 2.12 to:

$$s(r,t_n) = \left(\rho_{water}(r) + \rho_{fat}(r)\left[\sum_{i=1}^{M}\beta_i e^{j2\pi\Delta f_{cs_i}t_n}\right]\right)e^{-\varphi(r)t_n}, \quad n = 1, \dots, N \tag{2.14}$$

Here, the fat signal is modelled using an M (usually 6) peak model, where Δf_{cs_i} is the chemical shift between the i^{th} fat peak and water (Hz), and $\beta_i > 0$ is the relative weight of each peak. However, this model would require N ≥ M+2 images to estimate the unknown parameters, which is not practical due to the increased scan time. In this way, it is assumed that βi are known. Thus, the number of unknown parameters remains the same as the single peak model[56] [57]. Consequently, only 3 images have to be acquired.

However, this multi-peak signal model doesn't account for T_2* decay. Although for many applications the T_2* decay may be neglected, for imaging with substantially shortened T_2*, it is important to consider the effects from both fat and T_2*, as they may interfere with the estimation of each other. Therefore, it is possible to estimate the R_2* map, i.e. R_2* =1/ T_2*, by including it in the signal

model[57] [58]. This can be done by modelling the B_0 field inhomogeneity and the T_2* decay in a complex field map term, by changing equation 2.13 to:

$$\varphi(r) = \left[{}^{1}/_{T_2^*(r)} - j2\pi f(r) \right] \tag{2.15}$$

In this way, the number of unknown parameters increases to 6, thus 3 images acquired at different TE values should be enough for obtaining all the unknown parameters. However, as the number of complex acquired images is equal to the number of unknown parameters, the estimation can be very sensitive to noise. For a better performance, typically 6 echoes are acquired. Furthermore, for pseudo-CT generation, besides the importance of the R_2* estimation for water-fat decomposition, some studies prove the correlation between R_2* values and HU values, especially in bone tissues. This is mainly due to the correlation between R_2* values and bone mineral density, since bone minerals as calcium create local inhomogeneities that are reflected by R_2* values [27].

The model in equation 2.14 can be written in a matrix form as:

$$\underbrace{\begin{bmatrix} e^{-(\varphi(r)t_1)} & e^{-(\varphi(r)t_1)}\left(\sum_{i=1}^{M}\beta_i e^{-j2\pi\delta_i t_1}\right) \\ e^{-(\varphi(r)t_n)} & e^{-(\varphi(r)t_n)}\left(\sum_{i=1}^{M}\beta_i e^{-j2\pi\delta_i t_n}\right) \end{bmatrix}}_{A_\varphi} * \underbrace{\begin{bmatrix} \rho_{water} \\ \rho_{fat} \end{bmatrix}}_{g} = \underbrace{\begin{bmatrix} s[1] \\ s[N] \end{bmatrix}}_{s} \tag{2.16}$$

The unknown parameters are obtained by minimizing the least-square errors between the model and the measured data:

$$\{\rho_{water}, \rho_{fat}, \varphi\} = \arg\min_{\rho_{water},\rho_{fat},\varphi} \left\| A_\varphi g - s \right\|^2 \tag{2.17}$$

Since the above minimization is dependent on many parameters, the criterion is minimized with respect to some variables by assuming the other to be fixed, thus eliminating them from the optimization[59]. Minimizing the above cost function with respect to the concentrations, assuming φ to be fixed, we obtain the optimal concentration estimates as $g_{opt} = (A_\varphi^T A_\varphi)^{-1} A_\varphi^T s$. Replacing the optimal concentrations back in the previous cost function, and solving for φ, we obtain

$$\varphi(r) = \arg\min_{\varphi} \underbrace{\left\| A_\varphi \left(A_\varphi^T A_\varphi\right)^{-1} A_\varphi^T s(r) - s(r) \right\|^2}_{C(r,\varphi)} \tag{2.18}$$

In case of necessity of R_2* estimation, again it is possible to minimize the expression with respect to T_2* to obtain a cost function that is only dependent on *f*:

$$f(r) = \arg\min_{f} \underbrace{\min_{T_2^*} C(r,\varphi)}_{D(r,f)} \tag{2.19}$$

Since the estimation of T_2* values doesn't suffer from ambiguities, an exhaustive search over possible T_2* values can be performed to obtain *D* from *C*.

In order to address the sensitivity of the voxel-by-voxel optimization strategy described in equation 2.19 to multiple feasible solutions and phase wrapping, the joint recovery of the field map is formulated as a smoothness regularized optimization scheme. The global criterion is the linear combination of the sum of D and a smoothness penalty:

$$\hat{f} = arg\min_{f} \sum_{r} D\big(r, f(r)\big) + \mu \sum_{r} \sum_{\aleph(r)} \omega_{r,s} \, |f(r) - f(s)| \tag{2.20}$$

Here, ℵ(r) is the local neighbourhood of the voxel at location r, μ is an additional smoothing constant and $\omega_{r,s}$ are pre-defined weights that specify the relative importance of each difference term. The first term of equation 2.20 is the sum of the voxel independent criteria in equation 2.19, while the second term promotes field map smoothness. Then, the continuous problem is converted to a discrete optimization scheme by restricting the field map to a set of discrete values.

However, the direct discrete minimization of equation 2.20 is computationally infeasible, since it involves a large and fully connected graph, an iterative scheme where a one-layer graph is constructed and a sequence of binary decision problems at each iteration[60]. These decision problems are solved efficiently using a s-t graph cut algorithm. Thus, at $(n+1)^{th}$ iteration, there are two possible solutions at each voxel:$\Gamma_{n+1}(r) = \{f_n(r), g_n(r)\}$. Here, $f_n(r)$ is the optimal solution obtained from the previous iteration, while $g_n(r)$ is chosen as $f_n(r) \pm \beta$, where β may be a pre-specified constant, or a picked randomly among a set of local minimizers of D. This binary decision problem is efficiently solved using a s-t graph-cut algorithm[61], guarantying the solution to converge to a global minimum, obtaining in this way the field map (and, if it is the case, the R_2* map). Uploading this into the signal model represented by equation 2.14, it is possible to obtain the water and fat images.

2.2.2.2.1.2. Fat Fraction

As already discussed, quantification of the fat signal is important for pseudo-CT generation. The quantification can be done by calculating the relative amount of fat in a voxel[62], by using

$$FF = \frac{F}{F+W} \times 100 \tag{2.21}$$

where FF refers to fat fraction, F and W to the fat and water signal in a voxel, respectively.

Thus, the FF will present values between 0 and 100. However, if the true fat content is 0, any noise in the fat estimate will result in an FF>0. Thus, FF will be biased by noise[63]. This can be avoided by calculating the fat fraction as[55]:

$$FF = \begin{cases} \dfrac{F}{F+W} \times 100 & if\ W < F \\ \left(1 - \dfrac{W}{F+W}\right) \times 100 & if\ W > F \end{cases} \tag{2.22}$$

2.3. Estimating HU values from MR data

As previously mentioned, PET-MRI and MR-RTP lack electron density information to perform attenuation correction and dose calculations. This problem is commonly solved by the acquisition of an additional CT scan, which leads to systematic errors in the workflow caused by the imperfect MR-CT

registration. Thus, the estimation of HU values from MR data is a crucial step in PET-MRI and MR-RTP workflow.

Several approaches were developed to solve this problem. It is possible to group the several approaches into two main groups: anatomy-based approaches and voxel-based approaches[18]. The anatomy-based method generally uses a non-rigid registration between a library of MR reference images and a new patient MRI to warp a reference CT to match the anatomy of the new patient data[64] [65] [66] [67]. This method leads to significant errors when the new patient MRI geometry is very different compared to the geometry of the MR atlas[18]. The voxel-based method could be divided into two types. The first one involves a direct characterization into different tissue classes by manual segmentation followed by bulk assignments of HU values[68] [69]. The second one comprises a direct conversion of MRI voxels values to HU values by introducing a prior correlation between MRI and CT [17] [22] [23] [70] [71].

2.3.1. Anatomy-based methods

The anatomy-based method could be divided into two main approaches: the atlas-based method[64] [65] [66] [66] and the patch-based method[72].

2.3.1.1. Atlas-based method

The atlas-based method uses information from the whole image and can be divided in 3 steps, as illustrated in figure 2.6:

1. First, every CT and MR image from the atlas dataset are aligned using non-deformable registration (elastic deformation) to enable intra-subject alignment and producing multiple conjugated CT-MR atlas image pairs[64] [66].

2. Then, a registration between all MR atlas images and the MRI of a new patient is performed using non-deformable and deformable transformations, enabling the alignment between the MRI of the new patient and the MR atlas[64] [65].

3. The transformation matrices and deformation fields used in step 2 are also applied to the CT images in the atlas, building the pseudo-CT, according to different strategies of atlas fusion for HU value assignment [64] [65].

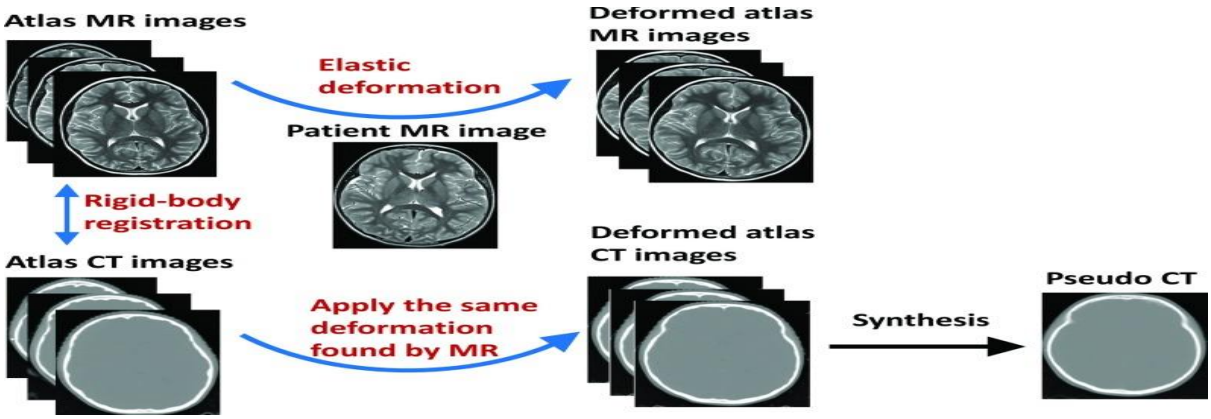

Figure 2.6 – Workflow of an atlas-based approach to generate a pseudo-CT [64].

The HU value for each voxel in the obtained pseudo-CT can be obtained using a simple mean process[64] [66] or a weighted average based on similarity measures[67].

Using a simple mean process, the pseudo-CT intensity (μ) of a voxel at the position x_0 is calculated using the mean of those at the same location in all deformed CT images in the CT atlas[64]:

$$\mu(x_0) = \frac{1}{Na} \times \sum_{i=1}^{Na} y_i(x_0) \tag{2.23}$$

Where Na is the number of atlases and y_i the HU value in all CT images in the atlas.

In the weighted average based on similarity measures method, the MRI of the new patient is matched with the MRI atlas database using deformable registration and local image similarity measures such as the local sum of squared differences (NSSD) and the structural similarity index extended to regions of interest (ROI-SSIM). The similarity results are ranked across all MR images in the atlas according to the quality of the registration. The ranks in each n^{th} subject and each voxel $\vec{v}$, $R_{n\vec{v}}$, are then converted to weights, $W_{n\vec{v}}$. Better registration results lead to a higher weight by applying a negative exponential decay function[67]:

$$W_{n\vec{v}} = e^{-\beta \times R_{n\vec{v}}} \tag{2.24}$$

Where β is a constant weighting factor. Then the intensity at each voxel of the pseudo-CT is calculated using

$$I_{\vec{v}}^{pCT} = \frac{\sum_{n=1}^{Na} W_{n\vec{v}} \times J_{n\vec{v}}^{CT}}{\sum_{n=1}^{Na} W_{n\vec{v}}} \tag{2.25}$$

Where $J_{n\vec{v}}^{CT}$ is the atlas CT image from subject n at voxel $\vec{v}$.

2.3.1.2. Patch-based method

The patch-based method involves the use of a rigidly aligned CT-MRI atlas as database but it excludes the use of deformable registrations. In this method, 3D patches are extracted from the target MRI followed by a spatial local search of the most intensity similar patches in the MRI database[72]. Thus, the use of deformable registrations is replaced by the patch resemblance search.

The patches extracted from the MRI atlas are centred on an arbitrary spatial location x, $P_S(x)$, and the HU value on position x in the aligned CT is designed by $T_S(x)$. Then, using this database, an intensity based nearest neighbour search is performed using:

$$d(s,x) = \|P(y) - P_S(x)\|^2 \tag{2.26}$$

where P(y) represents the patch at the target MRI. Then, the search is done aiming at finding the patch that minimizes $d(s,x)$. After this search, the corresponding HU value in the CT atlas at the same spatial location is stored as $T_{sk^{min}}(x_k^{min})$. Then, the HU value in the pseudo-CT at position y is calculated using a weighted average:

$$pCT(y) = \frac{\sum_k w_k \times T_{sk^{min}}(x_k^{min})}{\sum_k w_k} \tag{2.27}$$

Where the weights, w_k, are calculated by:

$$w_k = \exp\left(\frac{-d(s_k^{min}, x_k^{min}}{\min_k d(s_k^{min}, x_k^{min}}\right) \quad (2.28)$$

2.3.2. Voxel-based methods

2.3.2.1. Manual Bulk Density Assignment

The application of bulk density to MRI consists of the assignment of a single HU value to each tissue. HU values may be assigned to the entire body region, creating a homogeneous pseudo-CT, or to specific manually segmented volumes, creating a stratified pseudo-CT. Three sets of pseudo-CTs with increasing level of heterogeneity are commonly generated, as described in figure 2.7[68] [69]:

1. MRI_u: Delineation of the body contour, assigning the body as made of soft tissue.

2. MRI_b: Bone segmentation is also performed, assigning a corresponding single HU value to the bone, and the remaining anatomy is assumed to be soft tissue.

3. $MRI_{b,c}$: Adding to point 2, air segmentation is performed assigning the corresponding bulk HU value.

Figure 2.7 – Several Types of manual bulk density assignment [68]

2.3.2.2. Direct Voxelwise Conversion

Instead of manually segment different tissue types and assigning bulk HU values, which leads to an increased workload to the clinicians, the pseudo-CT can be obtained using a direct conversion of MRI values into HU value, adopting a patient specific tissue modelling by finding a prior correlation between MRI intensity signals and HU values. However, this approach faces some difficulties once there is no distinction between the MR signal in cortical bone and air when using conventional MR pulse sequences. This is due to the short T_2* relaxation time of cortical bone, making the signal to quickly

disappears, and the low proton density of air. Thus, both areas appear as dark in a MRI. To overcome this problem, UTE sequences were developed[19].

In UTE imaging, the signal is sampled during the FID, allowing the acquisition of the MR signal in the cortical bone before the signal vanishes. Thus, this pulse sequence uses TEs ranging between 0.008 ms and 0.15 ms, being 10 to 200 times shorter than conventional sequences, by using a hard-rectangular RF pulse with a small flip angle in combination with a radial, center-out k-space sampling. Here, the FID is mainly proton-density weighted, lack soft tissue contrast, but providing contrast between bone and air. In order to obtain more soft tissue contrast, the acquisition of another echo is needed. The addition of a new echo to the pulse sequence followed by its image subtraction from the first echo is called differential UTE (dUTE) imaging, enabling the distinction between short T_2* species (bone and air) and long T_2* species[25].

For the generation of pseudo-CTs using UTE sequences, automatic segmentation using bulk density assignment [25] or continuous model based methods may be used[17] [22] [23] [70] [71].

Regarding the bulk density assignment, a pseudo-CT may be constructed using dUTE imaging with 2 TEs, followed by the calculation of a R_2* map using equation 2.8. Then, a simple segmentation by thresholding is performed, segmenting the R_2* map into 3 tissue types: air, bone and soft tissue. Then, a bulk HU value is assigned to each one of the tissues creating a stratified pseudo-CT [25].

The use of continuous model based conversion methods relies on statistical models, describing the relationship between the voxel intensities in MR and CT data. The application of these statistical models involves using a set of CT and MR images co-registered to each other and resampled to the same resolution. Several statistical models were applied for pseudo-CT generation, namely a fuzzy c-means clustering technique and a Gaussian mixture regression procedure. For the first case, a dUTE sequence is acquired with three TEs. Then, an R_2* map is constructed using the first and third echo through equation 2.8. Also, a water-fat separation is also performed using a 2-point Dixon technique with the second and third echo, using equation 2.11. Then, for each image voxel, a probability between 0 and 1 of belonging to one of the tissue classes defined (air, bone, water and fat) is calculated. The pseudo-CT value of a voxel is then obtained by the product of the posterior probability of each voxel belonging to each one of tissue types defined and the mean HU value of each tissue class. The final pseudo-CT is obtained by summing the results across all classes. As a result, the probability weighted sum of the attenuation properties of each voxel yields an attenuation map capable of producing a pseudo-CT based on MR information of a new patient (figure 2.8)[17]. Regarding the use of a Gaussian mixture regression procedure, three sequences were acquired, two dual echo UTE sequences with different flip angles and one T_2 weighted spin echo sequence. Thus, five images are obtained. For each of the obtained images, two new images are derived by calculating the mean and standard deviation in a 27-voxel neighbourhood around each voxel, increasing the number of images to 16. Then, the joint distribution of these sixteen images and the CT image was calculated using a Gaussian mixture regression procedure (as explained in section 2.4), allowing the creation of a pseudo-CT[22].

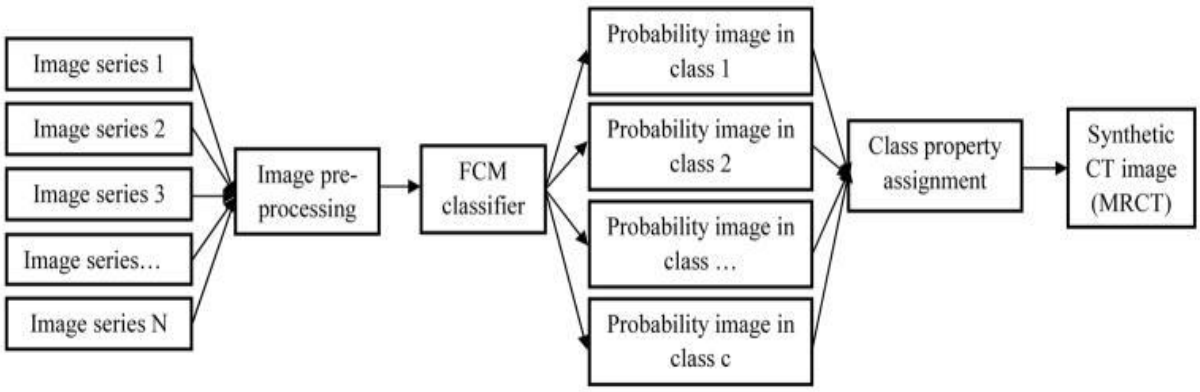

Figure 2.8 – Illustration of the workflow of pseudo-CT generation using a fuzzy c-means algorithm [21].

These methods were successfully applied to areas with a small FOV, such as the head and neck. However, its application in areas with larger FOV, such as the pelvic area, become difficult due to questions related to the hardware tweaking and noise considerations. Thus, some methods were developed using conventional sequences. These methods focus on developing a conversion model between the MR data and CT data, excluding the automatic bone segmentation as normally a manually segmentation of the bone is performed[73] [74]. Methods of bone segmentation such as anatomy-based segmentation or the development of a shape model of the bone can be added to the conversion models in order to obtain a fully-automated method. Furthermore, these methods usually consider the air in the rectum as soft tissue, due to the difficulty in segmenting it from areas with low T_1 relaxation time, such as the liquid in the bladder. However, it has been proven that the this fact doesn't introduce significant errors in dose calculation as well as attenuation correction[70].

One of these methods acquires three MR pulse sequences, namely: a 3D T_1 weighted Fast Field Echo (FFE) sequence, a 3D T_2-weighted turbo spin echo sequence and 3D balanced turbo field echo sequence[23]. Then after the manual segmentation of the bone anatomy (cortical bone and bone marrow), the voxel intensity in the resulting pseudo-CT is obtained using:

$$I^{pCT} = \sum_{i=1}^{3} w_i M_i \tag{2.29}$$

Where M_i represents the MR voxel intensity in the ith MR image acquired and w_i the weight assigned to it. This weight can be calculated using the following procedure:

1. The weights are initialized with random values
2. Pseudo-CT is generated
3. The difference between the obtained pseudo-CT and the CT is calculated
4. Minimization of the Euclidean Distance
5. Resulting weights are used to build the new pseudo-CT

Another method for generating a pseudo-CT for the pelvic area is based on a dual-model conversion method for the bone segment and for outside the bone segment, that are defined after manual segmentation, using a T_1/ T_2* -weighted sequence[70] [71]. For the model outside the bone segment, the MR image intensity was segmented into 3 classes, urine, fat and water, and the HU assignment for this area was made by linear interpolation. For the bone model, this method takes advantage of the complex relation between T_2* and HU, by generating a simplified model to explain it. First, the signal in the bone anatomy is normalized to the signal from water. Finally, a second order polynomial regression is

performed between the HU values in the bone and the normalized values. The result of this regression can then be applied to other subjects to obtain the bone pseudo-CT. The final pseudo-CT is generated by the simple overlapping of the two images obtained.

2.4. Gaussian Mixture Regression

2.4.1. Gaussian Mixture Model

The foundation for doing Gaussian mixture regression (GMR) is to model the joint density of the input/output (X/Y) space by a weighted sum of K multivariate Gaussian probability density functions (pdfs)[75]:

$$f_{X,Y}(x,y) = \sum_{j=1}^{K} \pi_j \phi(x,y;\mu_j,\Sigma_j) \tag{2.30}$$

Where π_j is a prior weight subject to the constraint $\sum_{J=1}^{K} \pi_j = 1$ and ϕ is a multivariate Gaussian pdf with mean $\mu_j = \begin{bmatrix}\mu_{jX}\\ \mu_{jY}\end{bmatrix}$ and covariance matrix $\Sigma_j = \begin{bmatrix}\Sigma_{jXX} & \Sigma_{jXY}\\ \Sigma_{jYX} & \Sigma_{jYY}\end{bmatrix}$. By definition Σ_j is symmetric so $\Sigma_{jXY} = \Sigma_{jYX}$. x and y are spatially corresponding voxel values in the input and output, respectively. Equation 2.30 represents a Gaussian mixture model (GMM). Each Gaussian, or component, in the model is sought to explain the distribution of a sub-population in the data.

The parameters $\theta_j = (\pi_j, \mu_j, \Sigma_j)$ of each Gaussian in the GMM are often not known in advance and needs to be estimated from the data at hand. A common way of doing this is by maximizing the log-likelihood function which explains the probability of the data given the parameters:

$$\hat{\theta} = \arg\max_{\theta}(p(X,Y|\theta) \tag{2.31}$$

The expectation maximization (EM) algorithm can be used to achieve this[76]. This optimization method iteratively estimates the maximum likelihood parameters from an initial guess of the parameter values. Although it is beyond the scope of this dissertation to go into details on how the EM algorithm optimizes the log-likelihood, this algorithm estimates the best parameters in two steps. Thus, the EM iteration alternates between performing an expectation step, which creates a function for the expectation of the log-likelihood evaluated using the current estimate of the parameters, and a maximization step, which computes parameters maximizing the expected log-likelihood found in the expectation step. Then, the estimated parameters are then used to determine the distribution of the latent variables in the next iteration of the expectation step. Furthermore, two important things should be noted about the method. Firstly, the EM algorithm cannot determine the number of components to use. This means that, for a good estimation of the GMM, one needs a prior knowledge of the number of components or sub-populations that exist in the data. Also, the EM method may converge to a local (and not global) maximum of the log-likelihood function depending on the initial starting point. Hence, the initial parameter guess is quite important as it may affect which optimum is found. In order to come up with a qualified initial guess on the composition of the components in the GMM, a k-means clustering algorithm can be applied to the data to make a rough estimation of $\hat{\theta}$ [77].

2.4.2. Regression using a Gaussian Mixture Model

Gaussian mixture regression (GMR) consists of a training phase and a test phase. When a decision has been made as to the number of components to use in the GMM, the training phase is, as described in the previous section, composed of estimating the parameters of the GMM using the EM algorithm. Once the GMM has been estimated, it can be used for regression. This is the test phase, which means the GMM is used on previously unseen input data, to make a prediction on the appearance of the output. To make predictions, the expected value of Y given an observed value of X=x should be found. From the definition of joint density, each Gaussian in equation 2.30, can be partitioned as the product of the conditional density of Y and the marginal density of X of each Gaussian:

$$\phi(x, y;\ \mu_j, \Sigma_j) = \phi\left(y \middle| x;\ m_j(x), \sigma_j^2\right)\phi(x, \mu_{jX}, \Sigma_{jXX}),\ \ j\ \in 1,2,\dots,K \tag{2.32}$$

Where

$$m_j(x) = \mu_{jY} + \Sigma_{jYX}\,\Sigma_{jXX}^{-1}(X - \mu_{jX}) \tag{2.33}$$

$$\sigma_j^2 = \Sigma_{jYY} - \Sigma_{jYX}\,\Sigma_{jXX}^{-1}\,\Sigma_{jXY} \tag{2.34}$$

are the conditional mean function and variance of Y. Inserting the result of equation 2.32 into equation 2.30 yields:

$$f_{X,Y}(x, y) = \sum_{j=1}^{K} \pi_j\, \phi\left(y \middle| x;\ m_j(x), \sigma_j^2\right)\phi(x, \mu_{jX}, \Sigma_{jXX}) \tag{2.35}$$

The condition density Y|X is now defined as

$$f_{Y|X}(y|x) = \frac{f_{X,Y}(x, y)}{f_X(x)} \tag{2.36}$$

Where

$$f_X(x) = \int f_{Y,X}(y, x)\, dy = \sum_{j=1}^{K} \pi_j\, \phi(x, \mu_{jX}, \Sigma_{jXX}) \tag{2.37}$$

is the marginal density of X. Inserting the definitions of $f_{Y|X}(x, y)$ and $f_X(x)$ into equation 2.36 finally yields:

$$f_{Y|X}(y|x) = \frac{\sum_{j=1}^{K} \pi_j\, \phi\left(y \middle| x;\ m_j(x), \sigma_j^2\right)\phi(x, \mu_{jX}, \Sigma_{jXX})}{\sum_{j=1}^{K} \pi_j\, \phi(x, \mu_{jX}, \Sigma_{jXX})} \tag{2.38}$$

This can also be expressed as:

$$f_{Y|X}(y|x) = \sum_{j=1}^{K} w_{j(x)} \phi(y;\ m_j(x), \sigma_j^2) \tag{2.39}$$

with the mixing weight

$$w_{j(x)} = \frac{\pi_j \phi(x; \mu_{jX}, \Sigma_{jXX})}{\sum_{j=1}^{K} \pi_j\ \phi\left(x, \mu_{jX}, \Sigma_{jXX}\right)} \tag{2.40}$$

The expected value of Y for a given X=x can now be found as the conditional mean function of equation 2.39:

$$E[Y|X = x] = m(x) = \sum_{j=1}^{K} w_{j(x)} m_{j(x)} \tag{2.41}$$

Equation 2.41 is the regression function in a GMR model and as can be seen, once the GMM has been established all the parameters needed for the regression are contained in equation 2.30. In other words, the crucial part of doing GMR lies in estimating a proper GMM. A simple example of GMR illustrating the steps involved can be seen in Figure 2.9[78].

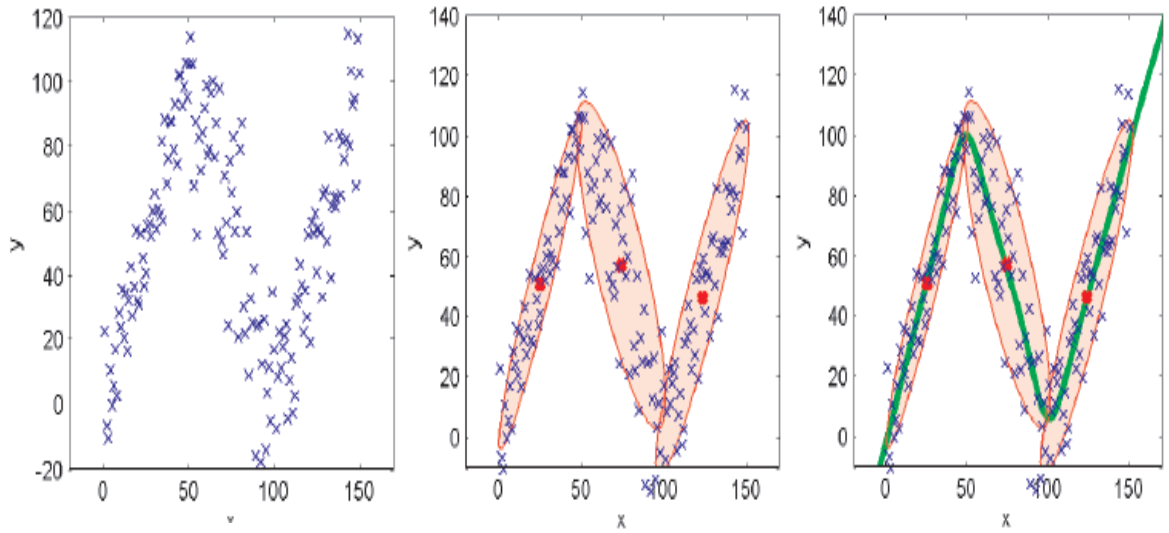

Figure 2.9 - Illustration of GMR using a simple univariate input and output**. Left**: Data generated by adding Gaussian noise to 3 linear functions. **Middle**: A GMM consisting of K=3 components is estimated using the EM algorithm with K-means initialization, mean values are marked as red dots. **Right**: GMR estimation of the expected value of y (green line) [78].

2.4.3. Impact of changing the number of components

Once the k-means algorithm is used with random seeds to make the initial parameter guess for the EM algorithm, the only parameter to tweak in GMR is the number of components to use in the GMM. As mentioned, ideally, one should have a prior knowledge of the number of sub-populations in the data in order to estimate a model that correctly explains the data. In the example in figure 2.9, it was known a priori that the regression problem consisted of three linear functions and, for these reasons, it made sense to use three components to model it. In figure 2.10, the impact of varying the number of components is illustrated. As can be seen, using too many components leads to over-fitting the data,

which is undesirable if noise is present. Also, over-fitting also leads to a more complex model, making more difficult the correct estimation of the model and the comprehension of it. On the other hand, using too few components leads to a higher degree of smoothing of the data, which may mean that important variations are missed. This is called under-fitting. Thus, the goal is to choose a model that is simple as possible by choosing the smallest number of components that can explain all the important variations in the data. However, with real-world multidimensional data, it can be difficult to know how many components should be used. A way to find the optimal number of components is to set up a measure of regression accuracy, evaluate different models and choose the one that performs best[78].

The Akaike information criterion (AIC) is a measure of the relative quality of statistical models for a given set of data[79]. Given a collection of models for the data, AIC estimates the quality of each model, relative to each of the other models. Thus, AIC can be calculated using

$$AIC = 2k - 2\ln(\hat{L}) \tag{2.42}$$

Where k is the number of components in GMM and $\hat{L} = p(X, Y|\hat{\theta})$, designed by likelihood. Given a set of candidate models for the data, the preferred model is the one with the minimum AIC value. AIC rewards goodness of fit (as assessed by the likelihood function), but it also includes a penalty that is an increasing function of the number of estimated parameters. The penalty discourages over-fitting, because increasing the number of parameters in the model almost always improves the goodness of fit. In this way, the simplest model as possible that can explain the data can be determined.

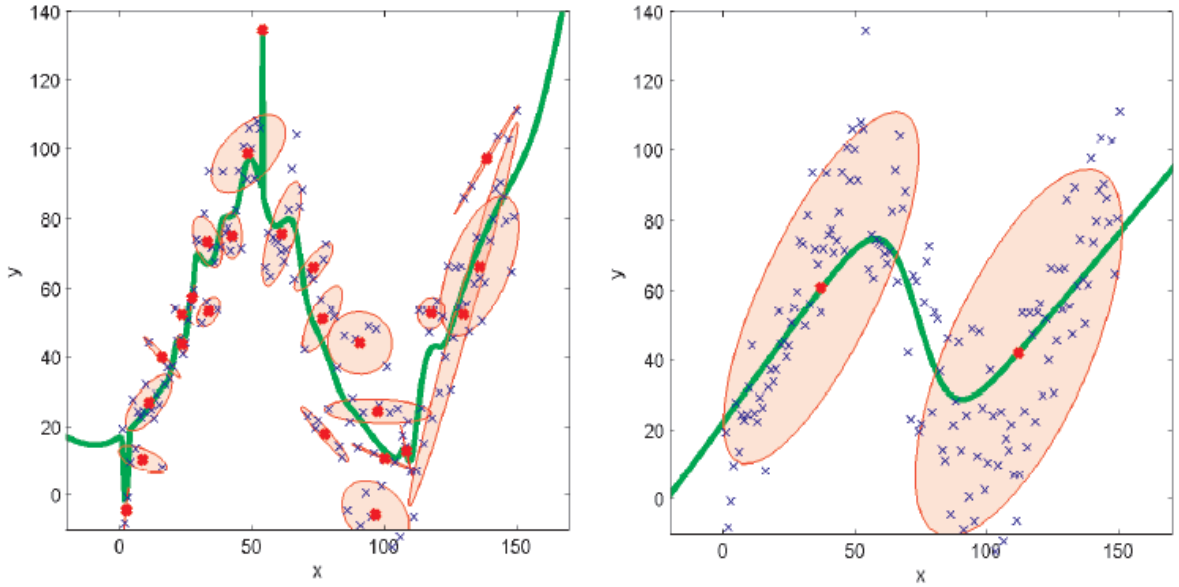

Figure 2.10 – Illustration of GMR using different number of components. Data is the same as in figure 2.9. **Left**: The GMM has been estimated using 25 components (over-fitting). **Right**: The GMM has been estimated using 2 components (under-fitting) [78].

Chapter 3

Methods and Materials

3.1. Data Specification

This study includes data from 6 anonymized prostate cancer patients (Patients 1 to 6). The datasets for each patient include a 3D CT image and a 3D MRI dataset, which were not acquired on the same day. Small discrepancies o the anatomy of the patient may be observed due to inter-scan variation caused by repositioning and the non-simultaneity of the acquisitions.

3.1.1. CT acquisition

Pelvic CT images were acquired using a Brilliance Big Bore (Philips Medical Systems, Best, The Netherlands) scanner operated at 120 KVp, with a 512 x 512 in-plane reconstruction. For patient 1, 1.28 x 1.28 mm^2 in-plane image dimensions with a slice thickness of 5 mm were used. For the remaining patients, 0.84 x 0.84 mm^2 in-plane image dimensions with a slice thickness of 5 mm were used. Specific immobilization devices, such as a knee wedge and a flat table top, were used during imaging.

3.1.2. MR acquisition

Pelvic MR images were acquired using an Ingenia 3.0 T system (Philips Medical Systems, Best, The Netherlands. A T_1-weighted Fast Field Echo sequence was acquired for all the patients using three echoes (TE=2.1/3.5/4.9 ms, TR=6.8 ms, Flip angle= 10°, Bandwidth=1122 Hz/pixel). The images were reconstructed with 336 x 336 x 75 matrix dimensions with an isotropic voxel size of 1.2 x 1.2 x 1.2 mm^3.

3.2. MR/CT Registration

The MR/CT image registration was done using the Elastix Registration software (Image Science Institute, Utrecht, The Netherlands)[80]. The MR data was considered as reference due to its smaller slice thickness. The process of registration was accomplished using two transformations, both using a mutual information algorithm.

First, in order to obtain a first alignment between the MR and CT data, the CT image was first registered using a rigid transformation[81]. However, due to inter-scan variation, some differences in patient's anatomy that could not be solved by a rigid registration were found.

Thus, a non-rigid registration was applied using a cubic bspline transformation[82]. However, bone anatomy is rigid and, therefore, a non-rigid registration cannot be applied to it, as it may cause unreal deformations. By applying a rigidity penalty, this problem may be solved[83]]. The rigidity penalty defines areas where the registration should be governed by a rigid transformation by including a binary mask of these areas as an input to the registration process. Thus, a bone binary mask was derived, using the following procedure, as illustrated in figure 3.1:

• First, a threshold of 100 HU was applied to the rigidly registered CT image in order to create a binary mask. Voxels with higher HU values were assigned with 1 and voxels with lower HU values were assigned with 0.

• A 2D morphological operation of removing objects with less than 5 connected voxels was applied to remove spurious voxels that were result of the thresholding[84].

• Finally, a hole filling 2D morphological operation was applied[84].

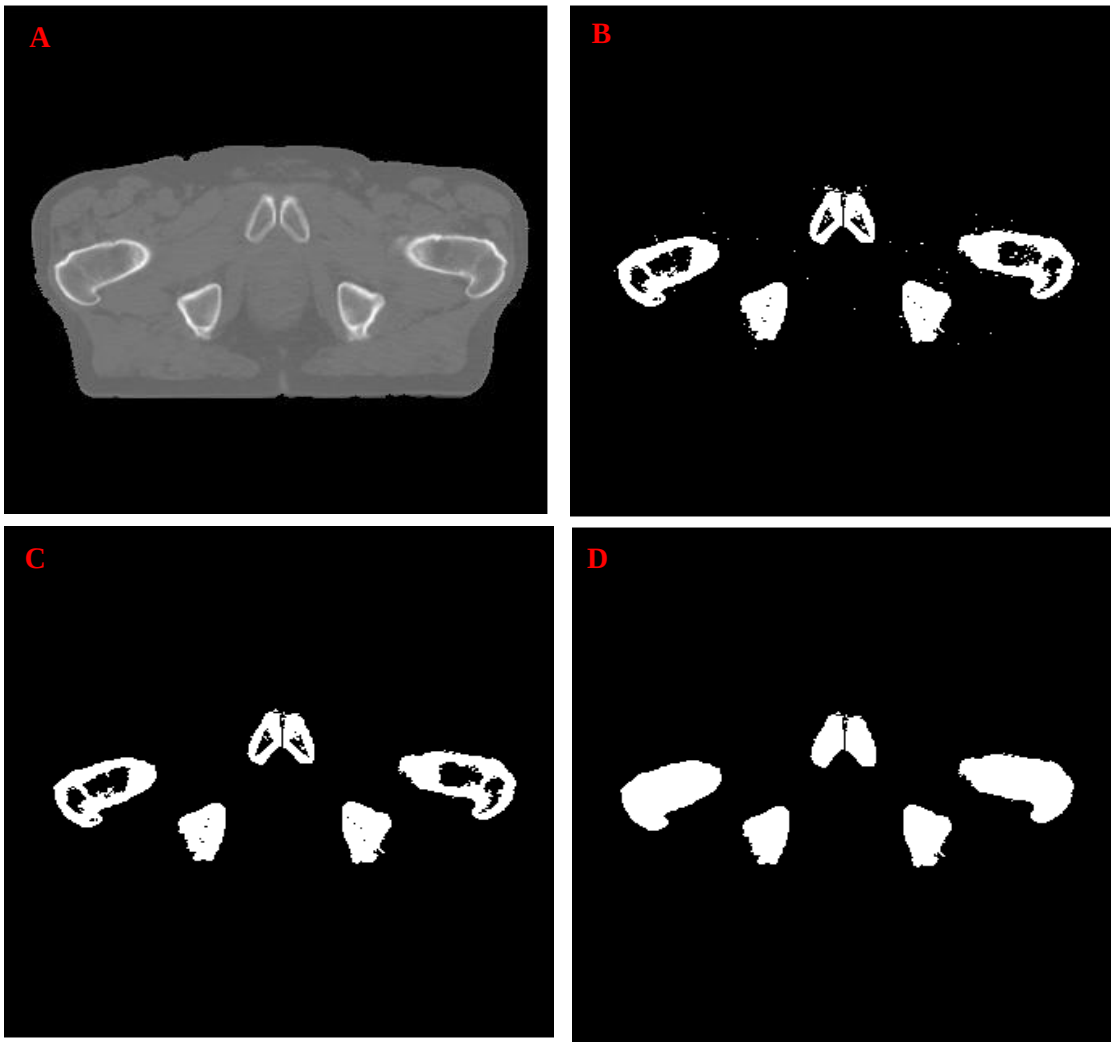

Figure 3.2- Representation of the derivation of the CT bone binary mask. **Figure 3.1-A** represents the CT image. **Figure 3.1 -B** represents the bone binary mask after the thresholding. **Figure 3.1-C** represents the binary mask after the removal of the spurious objects and figure **3.1-D** represents the final bone binary mask after the morphological hole filling operation.

The derived bone binary mask was used as input in the non-rigid registration with a rigidity penalty. In this way, the voxels included in the binary mask were subjected to a rigid transformation, while the registration in the remaining voxels was governed by a cubic bspline transformation.

The result of this registration was evaluated by visual inspection and the resulting CT image was saved for further evaluation.

3.3. Water/Fat Decomposition and R_2* estimation

The MR water-fat decomposition in the acquired MR images was performed using the graph-cut algorithm explained in section 2.2.2.2.1.1, by using the MATLAB (The Mathworks, Natick, MA) code provided by the Water-Fat decomposition toolbox, that was the result of the ISMRM Workshop on Water/Fat decomposition, that took place in California, United States of America in 2012[85]. This toolbox provides code for several water-fat decomposition algorithms, as well as code for evaluating the noise performance of the algorithm. The use of the water-fat decomposition by using a graph-cut algorithm was chosen among the available algorithms once it was demonstrated to obtain an accurate water-fat decomposition within a reasonable time.

The algorithm was performed without including the R_2* estimation. Forty iterations were used. The original code was modified and partially parallelized to allow the estimation of a multi-slice water-fat decomposition. Furthermore, in order to improve the speed performance and under the assumption that the field map varies smoothly, before the field map estimation, the original MR images were downsampled from a factor of 4. The obtained field map was then upsampled using the same factor. This field map was then used for the calculation of the water and fat images. The input parameters are detailed in Appendix I. The existence of water-fat swapping was assessed by visual inspection of the water and fat images.

The noise performance of the water-fat decomposition was also evaluated. The noise performance of a water-fat decomposition algorithm can be described by the effective number of signal averages (NSA), defined as[86] [87]:

$$NSA = \frac{\sigma^2}{\sigma_P^2} \tag{3.1}$$

Where σ^2 is the variance of the noise in a source image and σ_P^2 is the variance of the noise in a calculated water or fat image.

After the calculation of the water and fat images, two different features were calculated based on these images: in-phase image and a quantitative fat-fraction (FF) image. The FF image was obtained using equation 2.22 while the IP images were obtained using:

$$IP = W + F \tag{3.2}$$

The R_2* image of each patient was calculated using a mono-exponential fit with the first and third echo images, according to:

$$\frac{1}{T_2^*} = R_2^* = -\frac{\log S(TE_3) - \log S(TE_1)}{TE_3 - TE_1} \tag{3.3}$$

Where $S(TE_3)$ represents the signal at $TE = TE_3$.

The R_2* image here calculated was specific for the TEs used in this work. For a true quantitative estimation of the R_2* values, the TEs should be in-phase[88]. Therefore, the R_2* images obtained in this work cannot be comparable to other studies using different TEs.

3.4. MR and CT masking

In order to exclude objects that don't belong to the pelvic area, such as arms and hardware fixations, a binary mask covering only the pelvic area was created.

The masking of the MR features was achieved using a slice-by-slice procedure, also illustrated in figure 3.2:

1. Selection of the IP image
2. Automatic Otsu's thresholding and creation of binary mask[89]
3. Morphological hole filling operation[84]
4. Connected component analysis and automatic removal of all objects, except the largest, creating in this way a binary body mask[84].
5. Multiplication of binary body mask with each MR-related image

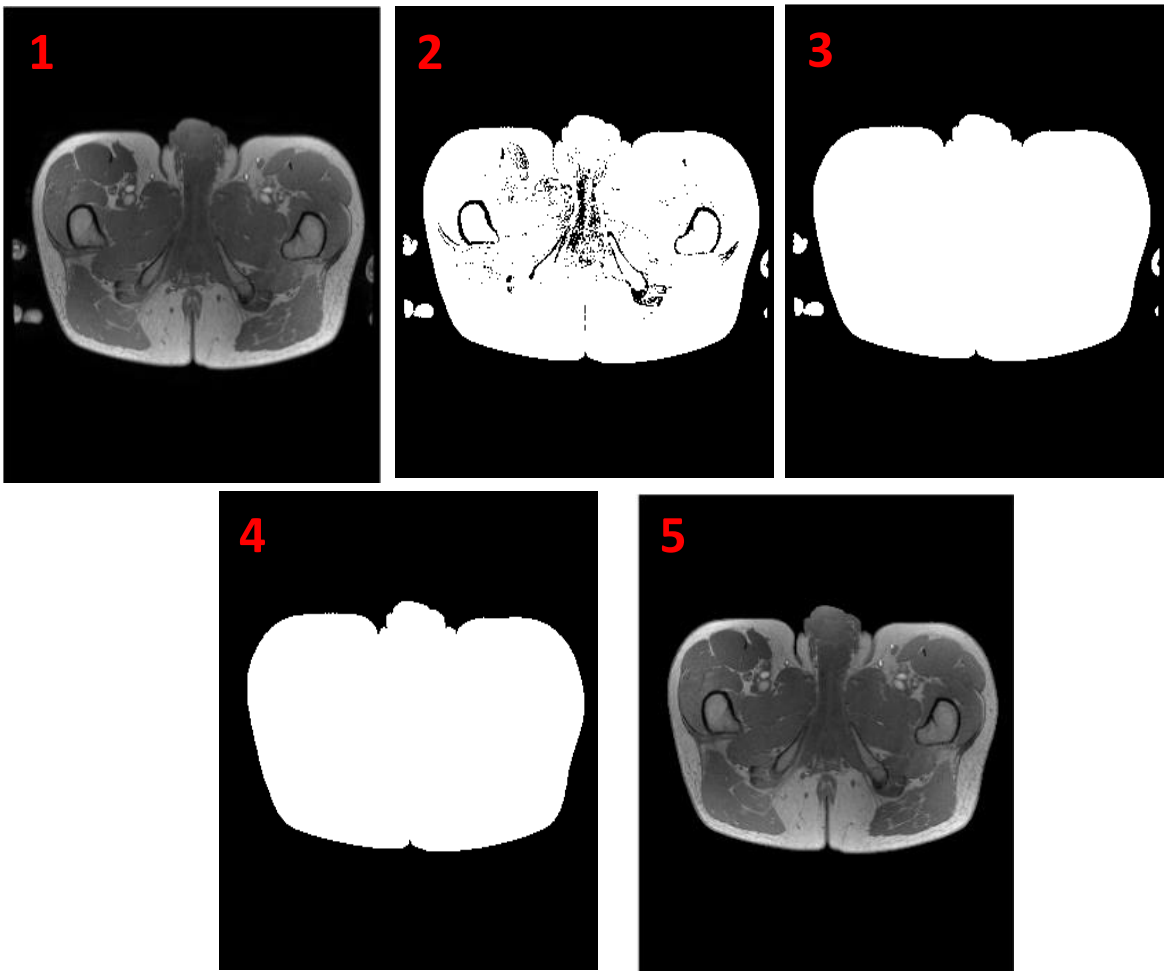

Figure 3.2 – Workflow of the masking in MR features.

The masking of the CT image was achieved using a similar approach. Here, the CT image replaces the in-phase image during the first step. Then, steps 2,3 and 4 were the same. In step 5, instead of a multiplication, the voxels outside the binary body mask were assigned with the value -1000 HU, characteristic of air.

3.5. Pseudo-CT generation and Validation

The pseudo-CT was generated using a dual-model regression approach. The first regression model was applied to the soft tissues and possible air, while the second was applied to the bone anatomy. This means it was necessary to have a segmentation of the bone anatomy.

The dual-model regression approach was validated using a Leave-One-Out-Cross-Validation (LOOCV) procedure. The dual-model was estimated from specific MR data and the corresponding CT data from five patients (training set) and applied to the same specific MR data of the remaining patient (validation set) to generate a pseudo-CT image. This procedure was repeated for all six combinations of training and validation data. The obtained pseudo-CT was then compared to the corresponding CT. The software to carry out the cross-validation procedure was developed in the context of this thesis in MATLAB 2016a.

3.5.1. MRI bone segmentation

The bone anatomy in MRI was manually contoured using the in-phase image. The manual segmentation is possible since the outer edges of the cortical bone, which appear as dark in the IP image, are clearly distinct from the surrounding outer tissue, as represented in figure 3.3. Thus, after the calculation of the in-phase image, this image was loaded into MeVisLab (MeVis Medical Solutions AG, Bremen, Germany) software, which enables the manually contouring of the bone anatomy. After this segmentation, the purple structure in figure 3.2 will construct a bone binary mask, while the remaining voxels inside the body mask will be part of the soft tissue binary mask.

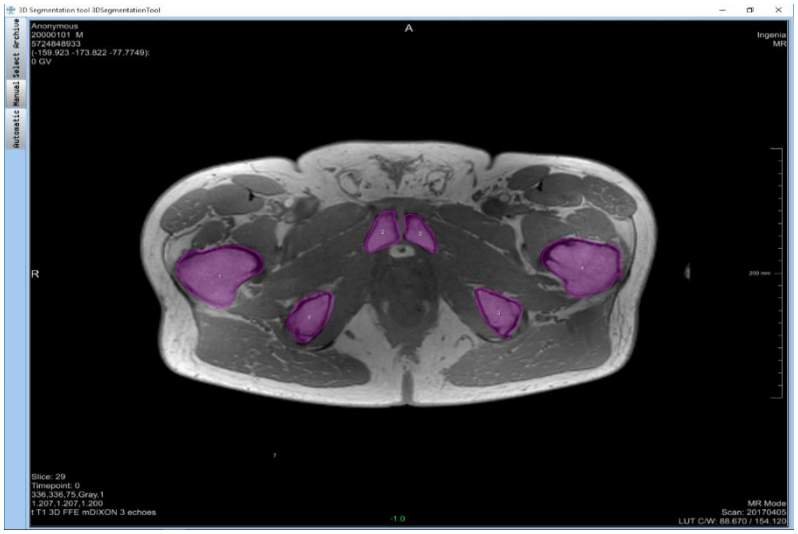

Figure 3.3 – Bone segmentation according the IP image using Mevislab. Purple structures represent the segmented bone anatomy.

The accuracy of the MR bone segmentation was evaluated by comparing its overlapping with the bone anatomy in the corresponding CT image. The segmentation of the bone anatomy in the CT image was performed using the same approach that was used in the MR-CT registration step, section 3.3, to derive the bone binary mask. The evaluation was done by calculating the Dice coefficient between the MR and CT bone masks[90]. The Dice coefficient is an index used to evaluate changes in size, position, orientation and shape between two overlapping volumes. A value of 0 indicates no overlap between volumes and a value of 1 indicates a perfect agreement. A good overlapping occurs when the value of

the Dice coefficient is higher than 0.7[91]. In the context of this work, the Dice coefficient was calculated as following:

$$Dice\ coefficient = \frac{2(Bone_{CT} \cap Bone_{MR})}{Bone_{CT} \cup Bone_{MR}} \quad (3.4)$$

Where $Bone_{CT}$ represents the bone mask in the CT image and $Bone_{MR}$ the bone mask that was manually segmented.

3.5.2. Soft tissue HU conversion model

The possibility to construct a pelvic soft tissue HU conversion model was investigated by comparing the quantitative FF values in soft tissue with the corresponding HU values in the CT image. As soft tissues are mainly constituted by water (muscle) or fat, a relative measure of the amount of water and fat signal within a voxel was considered sufficient. Possible existing air was also included in this model. The relation between FF values in soft tissue and HU values was obtained through a polynomial fit:

$$HU = a + b \times FF + c \times FF^2 + \ ... \quad (3.5)$$

Where a, b, c are the fitting parameters of the polynomial model and FF is the fat fraction in a voxel.

The order for the polynomial fit was chosen based on the minimization of the mean absolute error (MAE) between the obtained pseudo-CT and the real CT. Further description of MAE is provided in section 3.6.4. Thus, the LOOCV procedure was carried out for soft tissue areas using different polynomial orders. Then, the polynomial order that leads to a lower MAE was chosen to be used in the pseudo-CT generation procedure, and the results were saved for future application.

3.5.3. HU conversion model for bone anatomy

A MATLAB implementation of Gaussian mixture regression was used throughout this project[92]. This implementation used the built-in k-means function of the MATLAB Statistics toolbox to give an initial estimate of the component mean values and covariance matrices for the EM algorithm. EM was stopped when the increase in the log-likelihood value was smaller than 10^{-10}. The input variables (X) were MR related features while the output (Y) is the CT image. This toolbox was used instead of the MATLAB built-in functions due to its superior speed performance.

The R_2*, fat, water and fat fraction images that were previously calculated were included in the bone regression model. The inclusion of this set of variables as an intuitive explanation. The R_2* image provides information about the T_2* decay, which was proven to be correlated with the bone mineral density[17][24] [25] [26] [27]. Moreover, the FF image provides information about the relative presence of fat or water within a voxel and it was also proven to be correlated with the bone mineral density. At last, the water and fat images provide information about the signal intensity of these species when they are in-phase. As the MR sequence used in this project was a gradient-echo sequence type and the signal intensity is governed by the T_2* decay, the water and fat images can also provide information about it, at the same time that they provide information about the source of the signal.

Furthermore, for each variable included in the model, information about its neighbourhood was also included by calculating an image of the standard deviation of the 27-neighbourhood of each voxel. Thus, two different sets of variables were used for HU estimation in the bone:

- Model I: R_2*, Fat, Water and Fat Fraction
- Model II: R_2*, Fat, Water, Fat Fraction and an image of the standard deviation of 27-neighbourhood of each voxel from each original variable.

The impact of including neighbourhood information in GMR was assessed by comparing the MAE in the GMR that includes neighbourhood information to the MAE obtained when no neighbourhood information was included. The statistical significance of the improvement obtained by including the neighbourhood information was assessed by a one tailed t-test. A significance level of 0.05 was assumed. The null and alternative hypothesis were formulated as:

H0: MAE of GMR with no neighbourhood information is equal or lower than MAE with GMR with neighbourhood information

H1: MAE of GMR with no neighbourhood information is higher than MAE with GMR with neighbourhood information

The number of Gaussians to use in each model, with and without neighbourhood information, was calculated by calculating the minimum of the AIC, as described in section 2.4.3., for each model. The procedure for estimating the pseudo-CT for the bone anatomy is illustrated in figure 3.4.

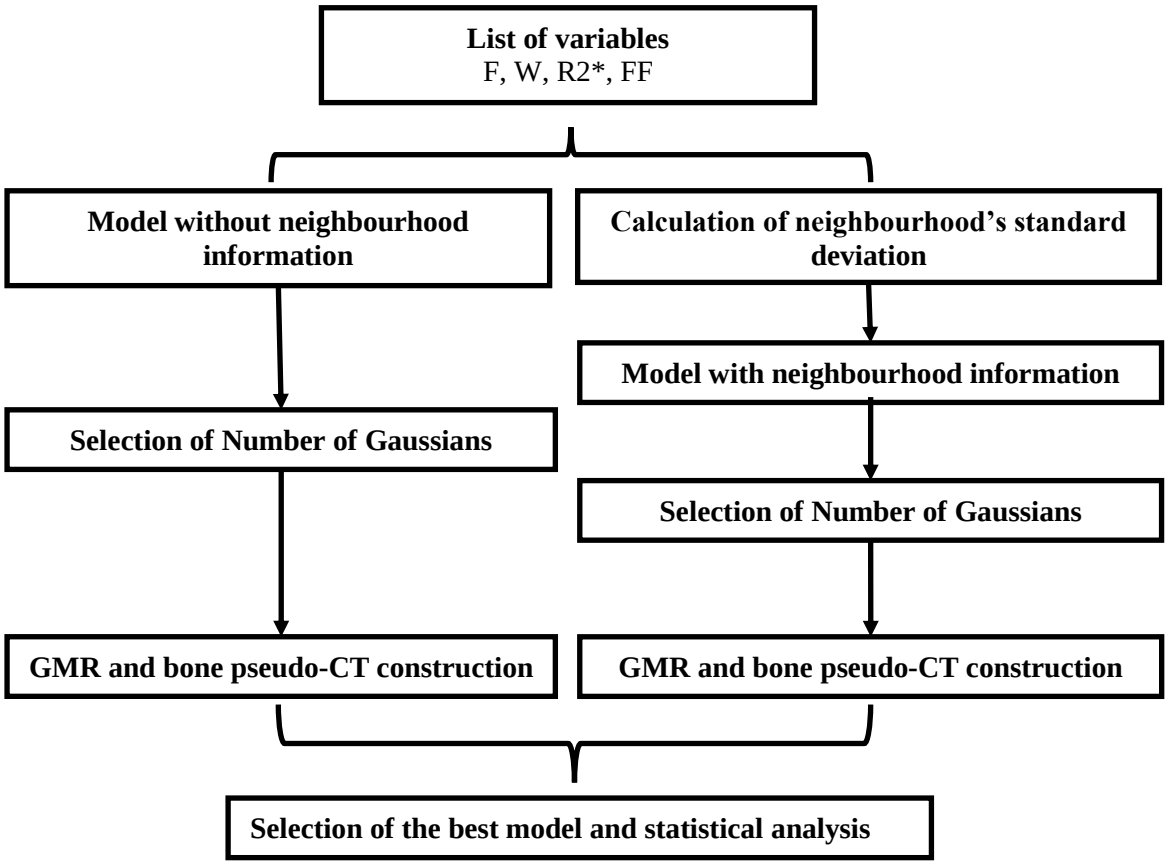

Figure 3.4 – Workflow of model selection and pseudo-CT construction in the bone using a GMR procedure. The left side of the scheme represents the pseudo-CT construction using a model which doesn´t include neighbourhood information, while in the right side, the workflow of generating a bone pseudo-CT through a model which includes neighbourhood information is explained.

3.5.4. Final Pseudo-CT generation and metrics of evaluation

The final pseudo-CT was obtained by overlapping the pseudo-CTs that were obtained for soft tissue and bone anatomy, according to sections 3.5.2 and 3.5.3, respectively. Due to the manual segmentation of bone, sharp edges in the bone anatomy contours may be present. To overcome this problem, the pseudo-CT was smoothed by applying a Gaussian filter with a standard deviation of 0.5[93]. Furthermore, the application of the Gaussian filter may allow a smoother transition between the overlapping of the intermediate pseudo-CTs. This procedure is illustrated in figure 3.5.

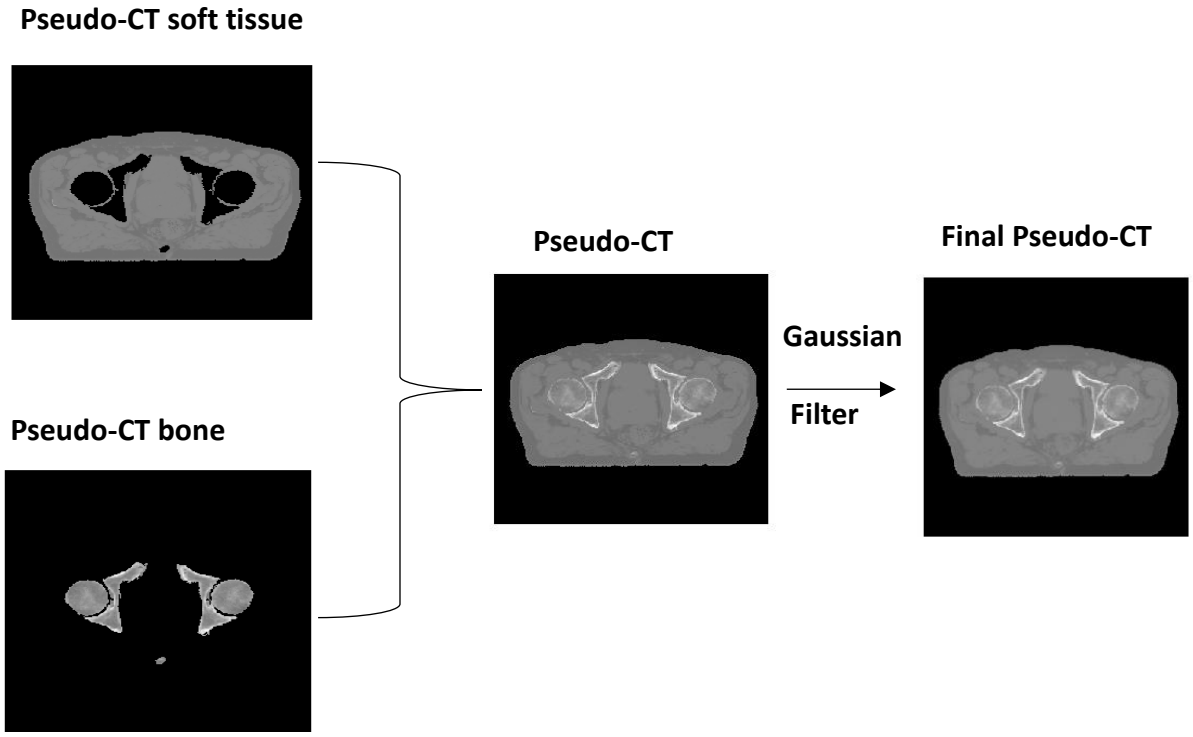

Figure 3.5 – Illustration of the workflow to obtain the final pseudo-CT. After estimating the dual-model regression parameters for soft and bone tissues, the resulting pseudo-CTs were overlapped. After, a gaussian filter is applied for smoothing.

The comparison between each pseudo-CT and the real CT was done using three different evaluation metrics. The first and main one was the calculation of the mean absolute error (MAE), which was also used for the optimization of the regression models[18]. A lower MAE indicates a better agreement between the pseudo-CT and the real CT. The MAE can be calculated by:

$$MAE = \sum_{i=1}^{N} \frac{|pCT(i) - CT(i)|}{N} \tag{3.6}$$

Where represents the number of voxels in the CT body mask.

To evaluate the presence of bias, especially, if the pseudo-CT is overestimated or underestimated, the mean error (ME) was also calculated by[23]:

$$ME = \sum_{i=1}^{N} \frac{CT(i) - pCT(i)}{N} \tag{3.7}$$

Furthermore, the peak signal.to-noise-ratio, PSNR, was also computed. This metric calculates the ratio between the maximum possible power of a signal or image and the power of corrupting noise that affects the fidelity of its representation. A higher value of PSNR represents a better reconstruction. PSNR is usually expressed in terms of the logarithmic decibel (dB) scale and it can be calculated by:

$$PSNR = 10\ \log_{10}\left(\frac{MAX^2(CT)}{MSE}\right) \tag{3.8}$$

Where $MAX(CT)$ represents the maximum HU value in CT image and MSE the mean squared error:

$$MSE = \sum_{i=1}^{N}\left(\frac{CT(i) - pCT(i)}{N}\right)^2 \tag{3.9}$$

Furthermore, the structural similarity (SSIM) index was also used for measuring the similarity between the pseudo-CT and the real CT. This metric, in contrast to the other methods, also incorporates perceptual phenomena, including both luminance and contrast in the calculation. Higher values of SSIM demonstrate a better agreement between the two images. SSIM can be calculated using:

$$SSIM(pCT, CT) = \frac{(2\mu_{pCT}\mu_{CT} + C_1)(2\sigma_{pCT,CT} + C_2)}{(\mu_{pCT}^2 + \mu_{CT}^2 + C_1)(\sigma_{pCT}^2 + \sigma_{CT}^2 + C_2)} \tag{3.10}$$

Where μ_{pCT}, μ_{CT} and σ_{pCT}^2, σ_{CT}^2 are the average and variance values of the pseudo-CT and CT, respectively, $\sigma_{pCT,CT}$ is the covariance between the pseudo-CT and the CT. $C_1 = (k_1 L)^2$ and $C_2 = (k_2 L)^2$ are two variables to stabilize the division, where L is the dynamic range of the pixel-values. By default, $k_1 = 0.01$ and $k_2 = 0.03$.

Chapter 4

Results and Discussion

4.1. Water-Fat Decomposition and R_2* estimation

Figure 4.1 shows the obtained maps by performing the water-fat decomposition without R_2* estimation. Figure 4.1-A and 4.1-B represent the fat and water-only images, respectively. As it can be seen in these figures, an accurate separation of the water and fat signal was achieved. Also, no water-fat swapping was found by visual inspection. Although no water-fat swaps were seen, some leakage of the fat signal into the water image was observed, as represented by the green arrow in figure 4.1-B. This leakage of the fat signal can be explained by the bipolar readout gradient that was used in this study to increase the scan efficiency and to allow the use of a shorter echo spacing, in order to eventually decrease the scanning time. When using bipolar readout gradients, the field map may comprise significant contributions from eddy currents caused by the bipolar readout gradient, that alternate with the readout gradient and thus violate the linear relation between the field map and TE assumed by a 3-echo method. An eddy-current correction method may be applied to correct for the presence of eddy-currents, but it was beyond the scope of this project[54]. Figure 4.1-C represents the field map obtained. As, a smooth field map was obtained, excepting for some tissue-air interfaces. The presence of air complicates the estimation of the field map. However, it did not result in water-fat swaps.

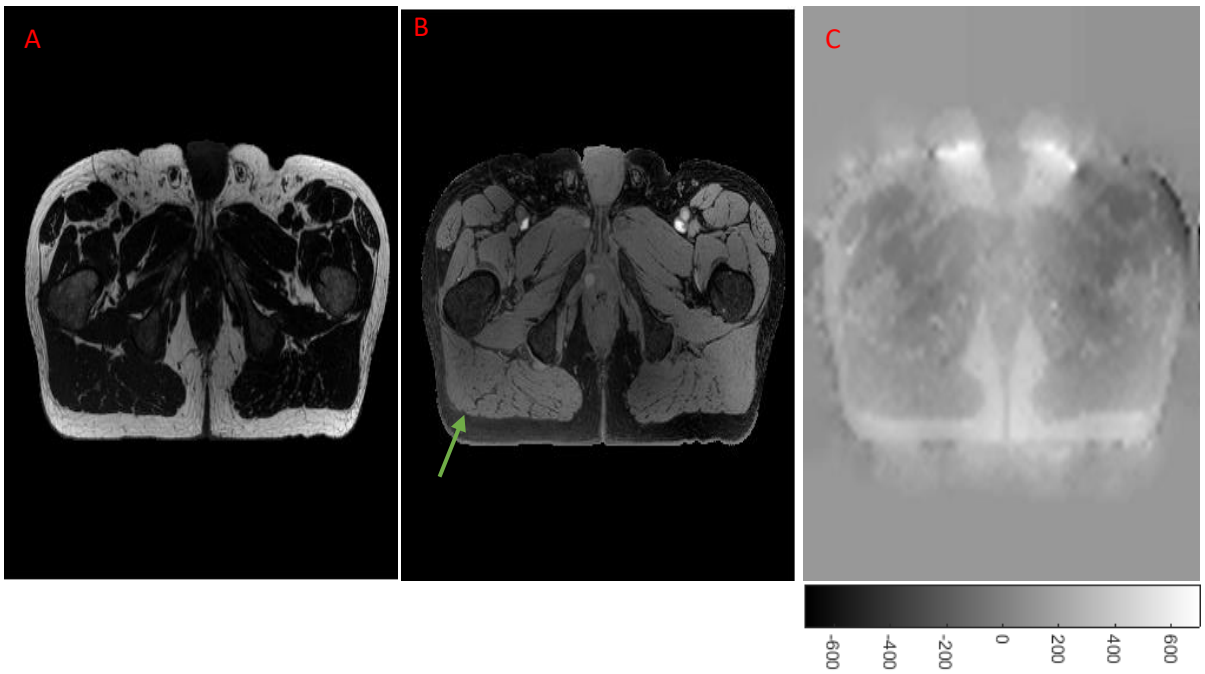

Figure 4.1 – Illustration of the results obtained through the water-fat decomposition algorithm without R2* estimation. **Figure 4.1-A** represents the fat image, **figure 4.1-B** the water image with the green arrow representing the effect of eddy currents and **figure 4.1-C** illustrates the obtained field map in Hertz. All these images are from patient 2.

The noise performance of this algorithm was also studied, by calculating the NSA map for the fat and water images, as illustrated in figure 4.2-A and 4.2-B, respectively. Theoretically, for a water-fat

algorithm that uses 3 echoes, the maximum value of NSA that can be obtained is 3, since only 3 echoes are used. As it can be seen in those figures, most voxels have values higher than 2 and close to 3. For the 6 patients used in this study, an average NSA of 2.64 ± 0.03 was achieved for the water images. Regarding the fat images, the average NSA was 2.66 ± 0.05 for the 6 patients. These values prove that the use of a graph-cut algorithm for water-fat decomposition without R_2* estimation has a noise performance close to the optimal values when only 3 echoes are used, proving the high SNR performance of this algorithm.

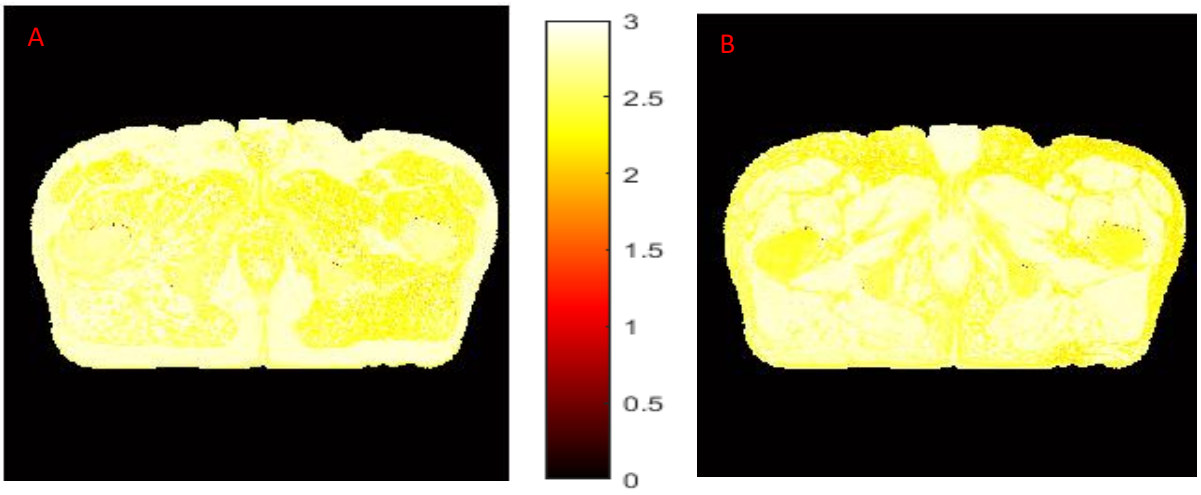

Figure 4.2- Illustration of NSA maps obtained for patient 2 when the water-fat decomposition algorithm is performed without R2* estimation. **Figure 4.2-A** represents the NSA map of the fat image, while **figure 4.2-B** represents the NSA map of the water image.

Then, the R_2* map was calculated, as it can be seen in figure 4.3. This R_2* map is specific for the TEs used in this project. Normally, an R2* value is specific for each tissue, regarding all the acquisition parameters, if the calculation is performed when the water and fat signal are in-phase. If this happens, the R_2* map can be used for the assessment of iron concentration among other applications[26]. The TEs of the first and third echo used in this study are not completely in-phase, causing the R_2* values to depend on the actual TE values. However, as it can be seen in figure 4.3, this "apparent" R_2* map is capable of providing contrast between the different tissue types. This is clearly visible from the figure 4.3, showing that water, fat and bone tissues present different R_2* values.

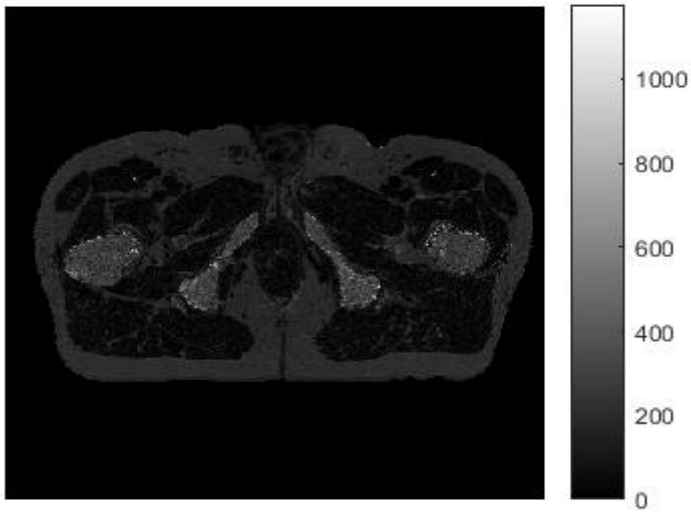

Figure 4.3 – Illustration of R2* map of patient 2. The R2* values are described in terms of ms^{-1}

A possible solution to estimate a "true" R_2* image relies on estimating it jointly with the water and fat images, by including it in the decomposition algorithm. As already referred, the water-fat decomposition algorithm allows the R_2* estimation. Theoretically, the simultaneous water-fat decomposition and R2* estimation may be performed using three echoes. However, in the presence of noise, the algorithm may become very unstable when only three images are acquired. Figure 4.4 illustrates the results obtained by using the water-fat decomposition algorithm that includes the R_2* estimation. It is possible to observe that the water and fat images, figures 4.4-A and 4.4-B respectively, present a noisier decomposition, especially the water image. In this image, we can see that the left part of the body presents more troubles, since the issues related to the leakage of the fat signal are even more visible. Also, the R_2* estimation is not accurate, since there are discrepancies in the estimated R_2* values for a single tissue type. It is well known that a single tissue type should have a homogeneous R_2* value. As it can be seen in figure 4.4-C, the R_2* values are different for the same tissue type, varying from the left part of the body to the right part. This discrepancy is especially visible in muscle, where in the left part of the body, the R_2* values are clearly distinguishable from the surrounding tissues, while in the right part, there is no contrast between the R_2* value of muscle and the R_2* values of the surrounding fat. It is also important to notice that, while in the water image it is the left part of the body that is more affected by the presence of noise, in the R_2* map it is the right part of body that presents these difficulties. The fact that the water-fat decomposition with R_2* estimation is noisier than the one performed without R_2* estimation is most likely caused by its high sensitivity to noise when only 3 echoes are collected. As referred before, each echo contributes with an imaginary and a real image. Thus, the number of input images to include in the water-fat decomposition algorithm is 6. If the R_2* estimation is included in the procedure, the number of unknows to estimate is 6 (real and imaginary fat, real and imaginary water, field map and R_2* map), while without R_2* estimation the number of unknows is only 5. Although theoretically, to obtain an accurate water-fat decomposition as well as the R_2* map, the number of input images has to be equal or higher than the number of unknows, this may not hold when noise is present. Thus, using 6 input images to obtain 6 unknowns may turn the algorithm very sensitive to noise. When only 5 unknowns are estimated, the remaining input image may be used for noise compensation. In this way, it can be concluded that for performing the R_2* estimation, the number of input images used in the algorithm has to be always higher than the number of unknowns to be estimated. Acquiring one more echo, it would be possible to estimate the R_2* map without having problems related to noise performance. However, this would increase the scanning time. In figure 4.4-D, we can see the obtained field map. This field map is similar to the field map obtained when no R_2* estimation is made. Since the field map estimation is the first step of the water-fat decomposition algorithm, it is less influenced by noise.

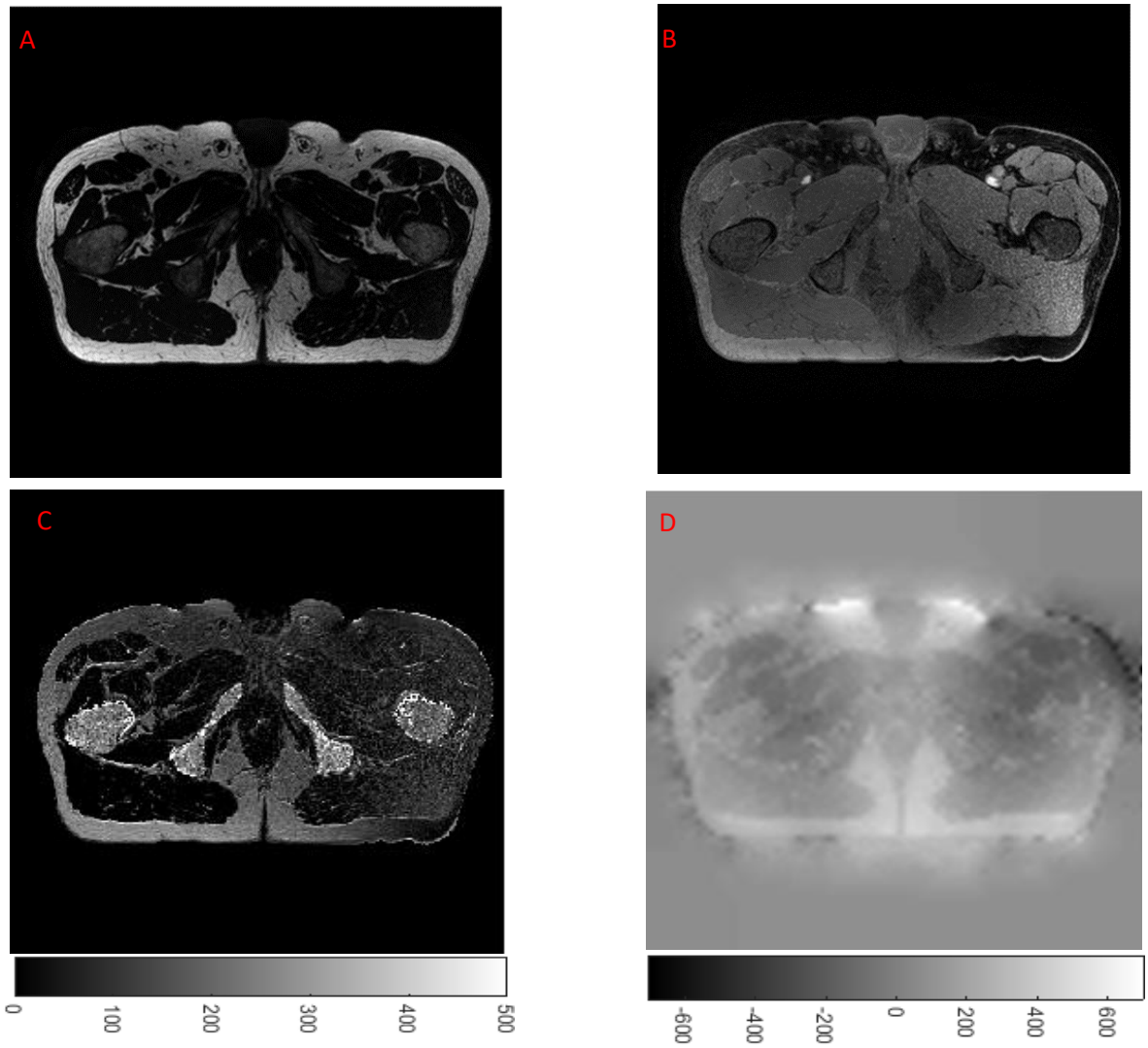

Figure 4.4 - Illustration of the results obtained through the water-fat decomposition algorithm with R2* estimation. **Figure 4.4-A** represents the fat image, **figure 4.4-B** the water image. **Figure 4-C** illustrates the obtained R2* map, while **figure 4-D** represents the obtained field map (Hertz). All these images are from patient 2.

The influence of noise in water-fat decomposition including the R_2* estimation was also evaluated by calculating the NSA maps of the water and fat images in order to evaluate the noise performance. Figures 4.5-A and 4.5-B illustrate these NSA maps of the fat and water images, respectively. It is visible that the NSA values for both images are significantly lower than the optimal value of 3 for 3-echoes water-fat decomposition algorithms[87]. An average NSA value of 1.18±0.07 for the NSA map of the fat image, while the average NSA value of the water image was 0.67±0.10. By comparing these NSA values with the ones obtained using the water-fat decomposition algorithm without R_2* estimation, it is possible to conclude that the inclusion of the R_2* estimation leads to a poorer noise performance when only 3echoes are included, as well as an inaccurate R_2* map.

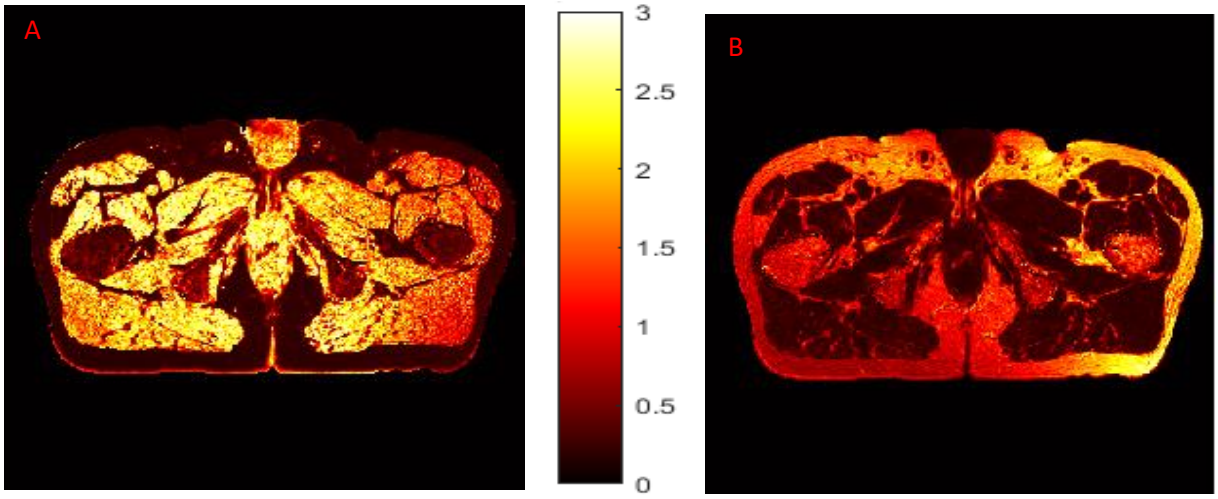

Figure 4.5- NSA maps of water and fat images of patient 2 when a water-fat decomposition with R2* estimation algorithm is performed. **Figure 4.5-A** represents the NSA map of the fat image, while **figure 4.5-B** illustrates the NSA map of the water image.

In this way, due to the poor noise performance as well as an inaccurate R_2* estimation of the water-fat decomposition with R_2* estimation algorithm, it can be concluded that the R_2* estimation is not possible to be performed jointly with the water-fat decomposition algorithm when only 3 echoes are acquired. As the goal of this project is to predict HU values through regression models, the "apparent" R_2* map was considered sufficient since it provides contrast between different tissues, as well as it describes the signal decay for the specific echo times used in this study. In this way, the "apparent" R_2* image was used for future application.

After obtaining the water and fat images, other features can be derived from the conjugation of these two images. The calculation of the fat fraction image is important since it provides a relative measure of the amount of the fat signal within a voxel. In this way, it is possible to find a relation between the relative amount of the fat signal and the HU values of fat and water, which will be important for the generation of the pseudo-CT. Figure 4.6 illustrates the obtained fat fraction image. Specifically, figure 4.6-A illustrates the calculation of the fat fraction which includes noise correction, while figure 4.6-B doesn't include the noise correction. Figure 4.6-C represents the absolute difference between these two images. As it is possible to see, figure 4.6-A has a homogeneous fat fraction within a single tissue type. In contrast, it is visible in figure 4.6-B that this homogeneity doesn't occur, since the fat-fraction values in muscle varies from the right side of the body to the left side, where the fat fraction values seem to be lower. This discrepancy can also be observed in figure 4.6-C, where the absolute difference between the fat-fraction images with and without noise correction is higher in the muscle in the left side than in the right side. Thus, it can be concluded that the calculation of the fat fraction image applying a noise correction can successfully correct for the presence of noise in tissues mainly constituted by water.

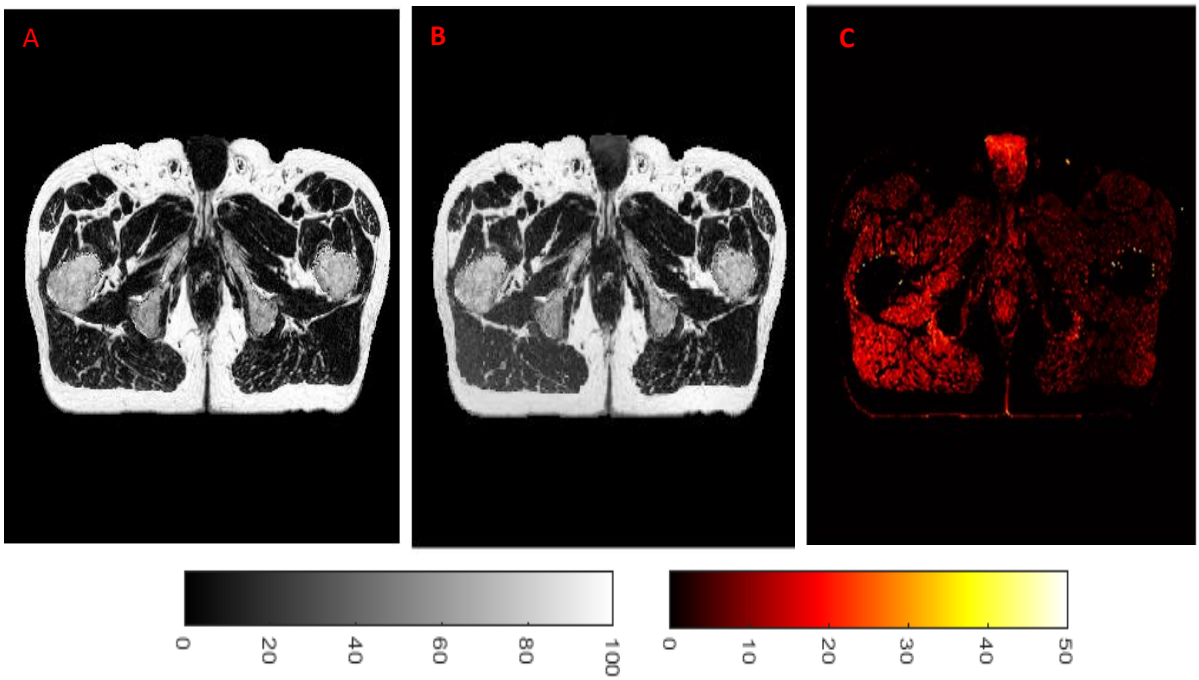

Figure 4.6 – Illustration of the fat fraction images obtained for patient 2. **Figure 4.6-A** represents the fat fraction obtained using a noise correction approach, while **figure 4.6-B** doesn't include the correction of the noise. Figure 4.6-C illustrates the absolute difference between figure 4.6-A and 4.7-B.

Furthermore, also the in-phase image was calculated based on the water and fat images. The in-phase image allows the distinction between low-signal and high-signal areas, as it can be seen in figure 4.7-A. In this figure, it is possible to see that the cortical bone appears as dark due to its fast T2* decay. This facilitates the manual segmentation of the bone, since there is a contrast between the outer edge of the cortical bone and the surrounding tissue, as it can be seen from the figure 4.7-B. In this figure, the signal profile along a line that crosses a bone structure (green line in figure 4.7-A) is represented, allowing to see the contrast between the outer edges of the bone structures and the surrounding tissue.

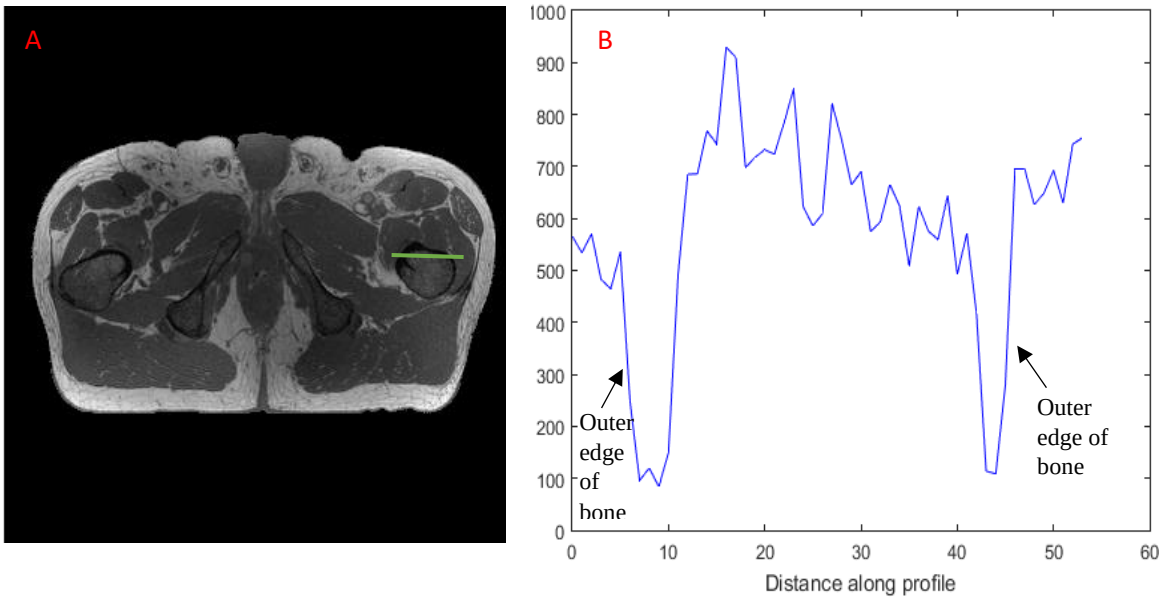

Figure 4.7 – Representation of in-phase mage obtained for patient 2 in **Figure 4.7-A**. The green line represents a row where the signal profile is represented in **Figure 4.7-B.** As it can be seen the outer edges of the bone structure crossed by the green line are clearly distinguishable from the surrounding tissue, allowing the bone segmentation.

The estimation of the water-fat decomposition related images, as well as the R_2* image was performed using an Intel 7 Core computer, with 2.6 GHz and 16 Gb of RAM, and for each patient, it had the duration of 217 seconds.

4.2. Pseudo-CT generation

4.2.1. MRI bone segmentation

The accuracy of the manual bone segmentation that was performed using the in-phase image was evaluated by calculating the Dice Score, having as reference the previously segmented bone anatomy in the CT image.

Figure 4.8 illustrates the obtained Dice Score per patient. An average Dice Score of 0.91±0.02 was obtained for all the patients, showing a good agreement between the bone segmentation in CT and MRI. The errors that were obtained may be explained by the natural ambiguity that the manual segmentation has, leading to imperfections when contouring the bone anatomy. Also, registrations errors are an important source of error, since a perfect alignment between the CT image and the MRI is almost impossible to obtain. Furthermore, the quality of the registration was assessed by visual inspection, leading to errors related to the subjectivity of the human condition. These contouring and registration errors will not be only important in the evaluation of the bone segmentation, but also in the subsequent steps of the pseudo-CT, since the errors are propagated throughout the whole pseudo-CT generation procedure.

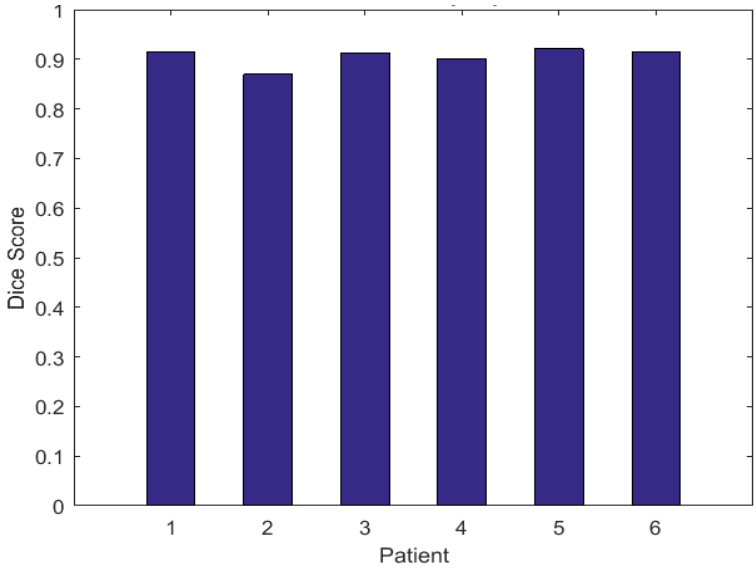

Figure 4.8 – Bone dice score per patient between the bone MR segmentation and the CT bone tissues

4.2.2. Soft tissue HU conversion model

As soft tissues are mainly constituted by water (muscle) and/or fat, a quantitative measure of the MR signal present in a voxel may be useful to estimate the HU values in soft tissues. As the fat fraction provides the relative amount of fat signal in a voxel, it may be used for HU estimation.

Thus, Figure 4.9 represents the joint histogram of the fat fraction and the HU units in the soft tissue mask. As it can be seen, most of the tissues with a lower fat fraction (FF<50%), representing tissues mostly constituted by water, have a HU between 0 and 100, which is the typical value for mainly consisting of water, such as the muscle. Also, fatty tissues (FF>=50%) have HUs between 0 and -100 HU, which again, is the typical values for these tissues in a CT image. Thus, a negative linear correlation between the HUs and fat fraction values can be found, having a Pearson Correlation Coefficient of -0.63.

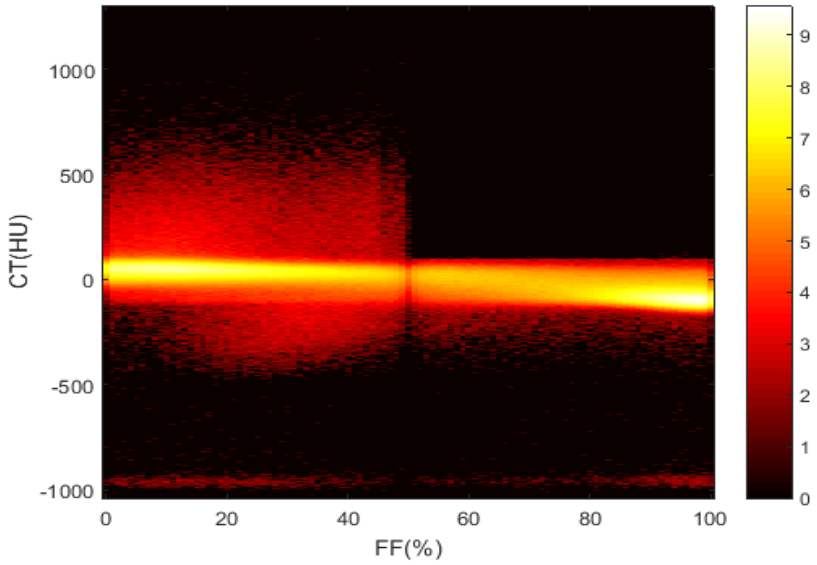

Figure 4.9 – Joint histogram between the fat fraction values and the HU values in soft tissue

Furthermore, in this joint histogram, it is possible to see the presence of high HU values, typical of bone, that are related to low fat fractions. The presence of these voxels in the soft tissue mask is due to the errors in the bone countering which makes that not all the bone tissues in CT are overlapped with the MR bone mask. Moreover, in the bottom of the joint histogram it is possible to see the presence of air in the CT images (-1000 HU). This air is located in the rectum. The inclusion of air voxels in the soft tissue model may be explained for several reasons. First, the urine in the bladder (with HU close to the water) presents a very long T_1 relaxation time, which makes it to appear as dark in T_1-weighted images. In this way, the distinction between the bladder and the air in the rectum becomes difficult. Also, as the MR and CT images were acquired at different time points and with different patient positioning, differences in the position and volume of the air in the rectum were observed. These differences would lead to higher errors when the air MRI and CT air does not overlap consistently. At last, for dose calculation and attenuation correction purposes, it was proven that the assignment of a soft tissue HU value to the air in the rectum during pseudo-CT generation didn't lead to significant errors[70]. However, if a bone HU value was assigned, the error in dose calculations and in attenuation correction calculations would be significant, proving the necessity of bone segmentation. Thus, it was decided to include air voxels in the soft tissue conversion model.

The order of the polynomial fit to use in the soft tissue regression model was chosen based on the minimization of the MAE in soft tissue using the LOOCV procedure. In figure 4.10-A, we can see the MAE per patient using the first four polynomial orders, while figure 4.10-B illustrates the average MAE per polynomial order. As it can be seen in these two figures, using the first polynomial leads to a higher MAE in all patients when compared to the others polynomial orders, which was proven to be statistically significant (p-value=0.002). In contrast, there was no statistical difference between the means of MAE

for each subsequent polynomial order (p-value=0.13). A level of significance of 0.05 was assumed for these tests. A second order polynomial fitting model was chosen to maintain the regression model as simple as possible, without compromising the results. An average MAE obtained for soft tissue using a second order polynomial regression was 33.61 ± 2.91 HU. In figure 4.11, it is possible to see an example of the pseudo-CT for soft tissue.

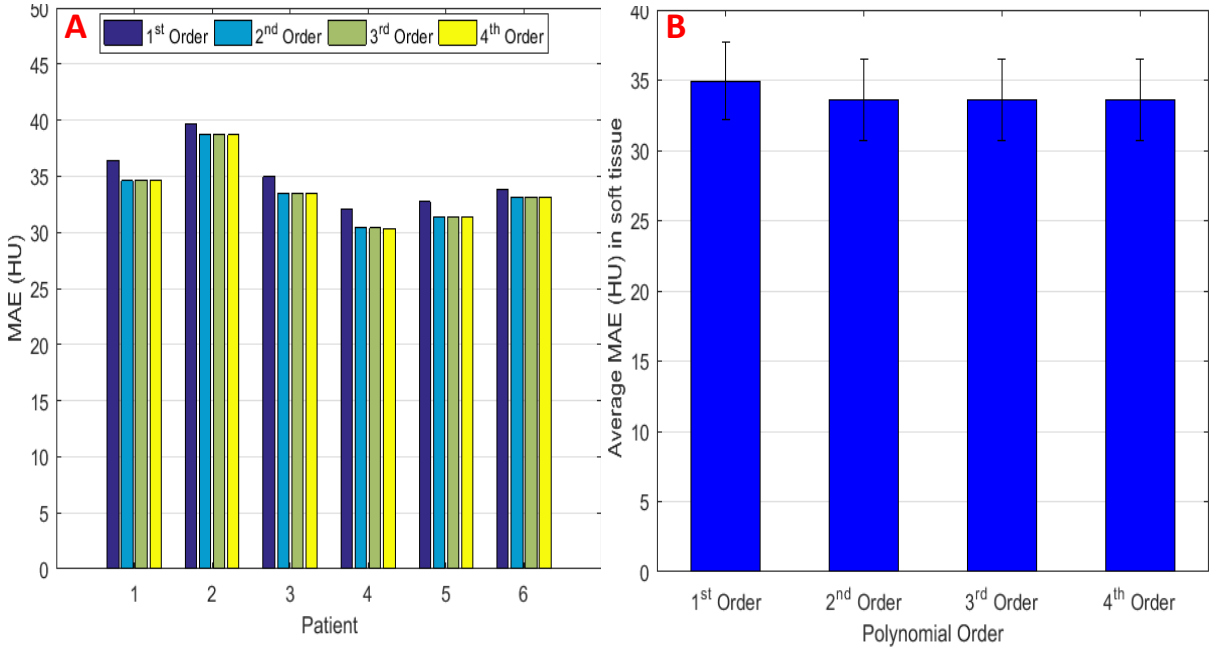

Figure 4.10 – Representation of the values of MAE in soft tissue. **Figure 4.10-A** represents the MAE of each patient while **Figure 4.10-B** represents the average MAE per polynomial order.

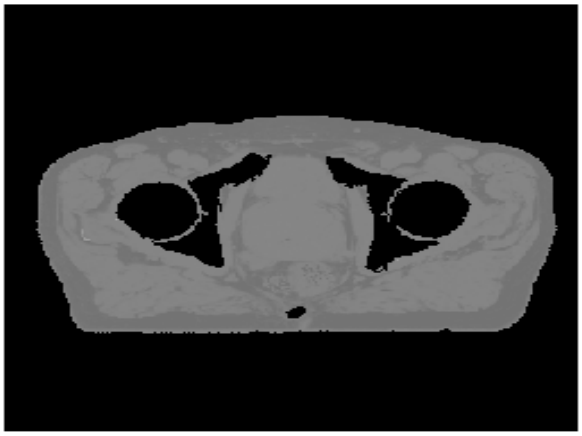

Figure 4.11 – Illustration of the pseudo-CT for soft tissue of patient 3. The black areas inside the body represent the bone anatomy.

4.2.3. HU conversion model for bone anatomy

The number of components (gaussians) to use in each GMM was assessed by the minimization of the AIC of each model using different numbers of components. Figure 4.12 illustrates the values of AIC for each model using different number of gaussians. As it is possible to see, the minimum value of the AIC of Model I is obtained when two gaussians are used, AIC=52.80, while, for the Model II, the

minimum value is obtained when three gaussians are used, AIC=86.70. In this way, Model I, which doesn't include neighbourhood information, is modelled by a mixture of two subpopulations. Since, in contrast to other bone tissues, there is no signal in the cortical bone, the existence of two subpopulations may be explained. Regarding Model II, which includes neighbourhood information by calculating the standard deviation of the 27-neighbourhood of each voxel of the MRI features, it is modelled by three populations. Thus, the inclusion of neighbourhood information may turn the distinction of another subpopulation of voxels possible. This may be explained by the fact that non-cortical bone tissues may be divided in bone marrow and cancellous bone, of which the cancellous bone has higher HU values. In this way, the inclusion of neighbourhood information is capable of modelling these different bone tissues.

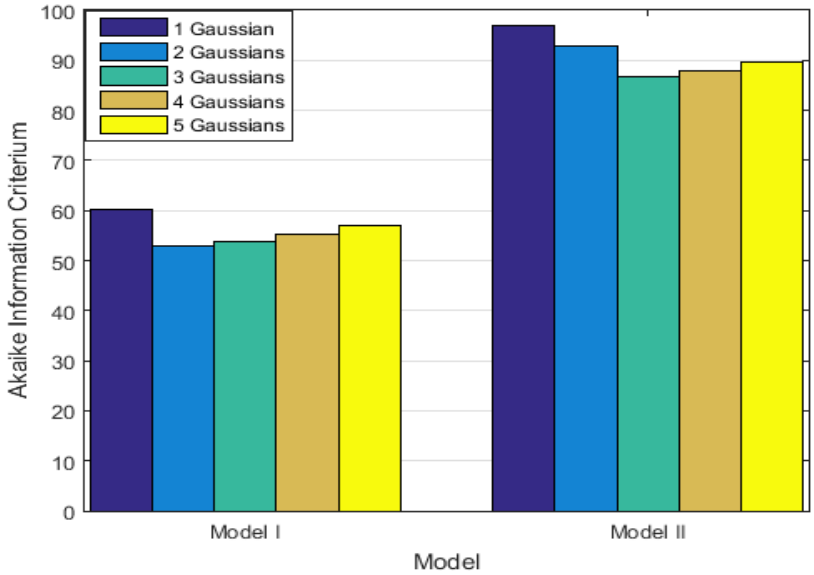

Figure 4.12 – Representation of AIC values for each model using different number of Gaussians in GMR. For Model I, the variability present in the model is sufficiently explained by a combination of two gaussians, while for Model II, three gaussians are required to explain its variability.

Figure 4.13-A and figure 4.13-B represent the MAE in bone anatomy for each patient and the average MAE in all the patients, respectively. As it is possible to see, Model II, which includes neighbourhood information, presents a lower MAE for every patient as well as a lower average MAE than Model I, which doesn't include the neighbourhood information. The average MAE of Model II was 101.49±10.80 HU, while the MAE obtained for Model I was 113.99±17.72 HU. Thus, it is possible to conclude that the inclusion of neighbourhood information in GMR leads to a significantly lower MAE, p-value=0.02, using a significance level of 0.05. However, the superior predicting performance of the the model including neighbourhood information may be related to the fact that more Gaussian components are used in the parameter estimation, which usually leads to an increase in the log-likelihood function, even though the AIC criterium suggests that two gaussians are sufficient to explain the variability in the model which doesn't include neighbourhood information. To depict for this possibility, the LOOCV was also performed for Model I using 3 gaussians. The average MAE, in this case, was 113.45±18.42 HU, which doesn't introduce significant improvements.

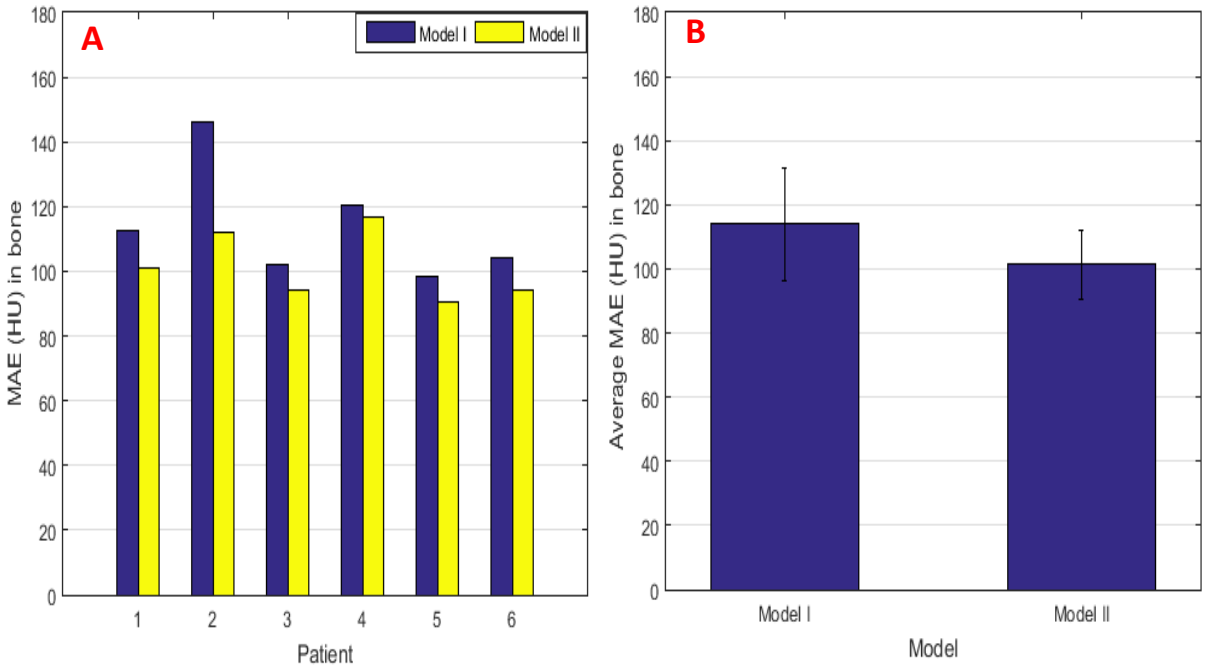

Figure 4.13 – Representation of the MAE for bone anatomy using different models. **Figure 4.13-A** represents the MAE for each patient and model used, while **figure 4.13-B** represents the average MAE using each model for bone anatomy HU estimation. As it is possible to see, Model II exhibits superior predicting performance in terms of MAE for all the patients used in this study.

Thus, Model II was chosen to be the best model and the results were saved for the generation of the final pseudo-CT. Figure 4.14 illustrates an example of the pseudo-CT for bone anatomy.

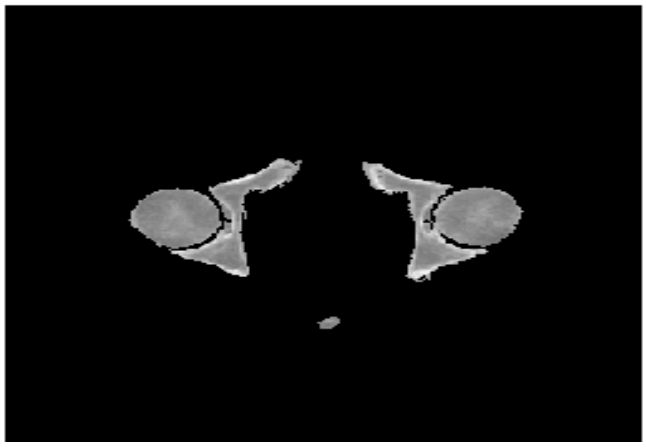

Figure 4.14 – Illustration of the pseudo-CT obtained for bone anatomy of patient 3.

4.2.4. Final pseudo-CT generation and evaluation

The final pseudo-CTs were generated by overlapping the obtained pseudo-CTs for soft and bone tissues of the same patient and smooth them with a Gaussian filter. As already referred, the pseudo-CT for soft tissues were obtained by using the LOOCV procedure applying a second order polynomial fit regression, and the pseudo-CT for bone anatomy by a GMR procedure using a model that includes neighbourhood information. In figure 4.15, we can see examples of slices of the obtained pseudo-CTs,

as well as the respective slices of CT and the absolute difference between the pseudo-CT and the CT. As it is possible to see, some differences between the pseudo-CT and respective CT.

The biggest difference is shown in the rectum as the air in rectum it was included in the soft tissue mask. Therefore, a soft tissue HU value was assigned to these voxels in the pseudo-CT. As referred before, this fact was proven to not introduce significant errors in dose calculations, as well as the calculations for attenuation correction[70]. However, it does influence other evaluation metrics, such as the MAE and the ME, suggesting results with less agreement to the CT image than if the air was treated separately.

Another important source of error comes from registrations errors. As it is possible to see in figure 4.15, some errors are placed in tissue/outside air and tissue/bone interfaces. Small errors during the registration step produce systematic errors that will propagate during the validation procedure. Although these errors are taken into account for the evaluation of the pseudo-CT generation, these errors will not be visible when the pseudo-CTs are applied in a MR-only workflow, since no MR-CT registration is needed, apart from the necessary to estimate the regression parameters.

Errors in the delineation of the bladder are also found. These errors are due to the fact that the MR and CT images were not acquired at the same moment. As result, there are some differences in the position and filling, that lead to the discrepancies between the pseudo-CT and CT.

Finally, it can be seen that the absolute error in bone anatomy is higher than in the remaining body of the patient. Also, it can be seen that higher the HU value in the CT image, higher the absolute error in those voxels, as it is also represented in figure 4.16. As the higher HU values represent the cortical bone, and as there is no signal is those areas in the MR images, the pseudo-CT cannot provide contrast within cortical bone voxels. Furthermore, it is also possible to see the errors in bone/tissue interfaces. These errors are due to registration errors, as well as imperfections during the manual segmentation of the bone.

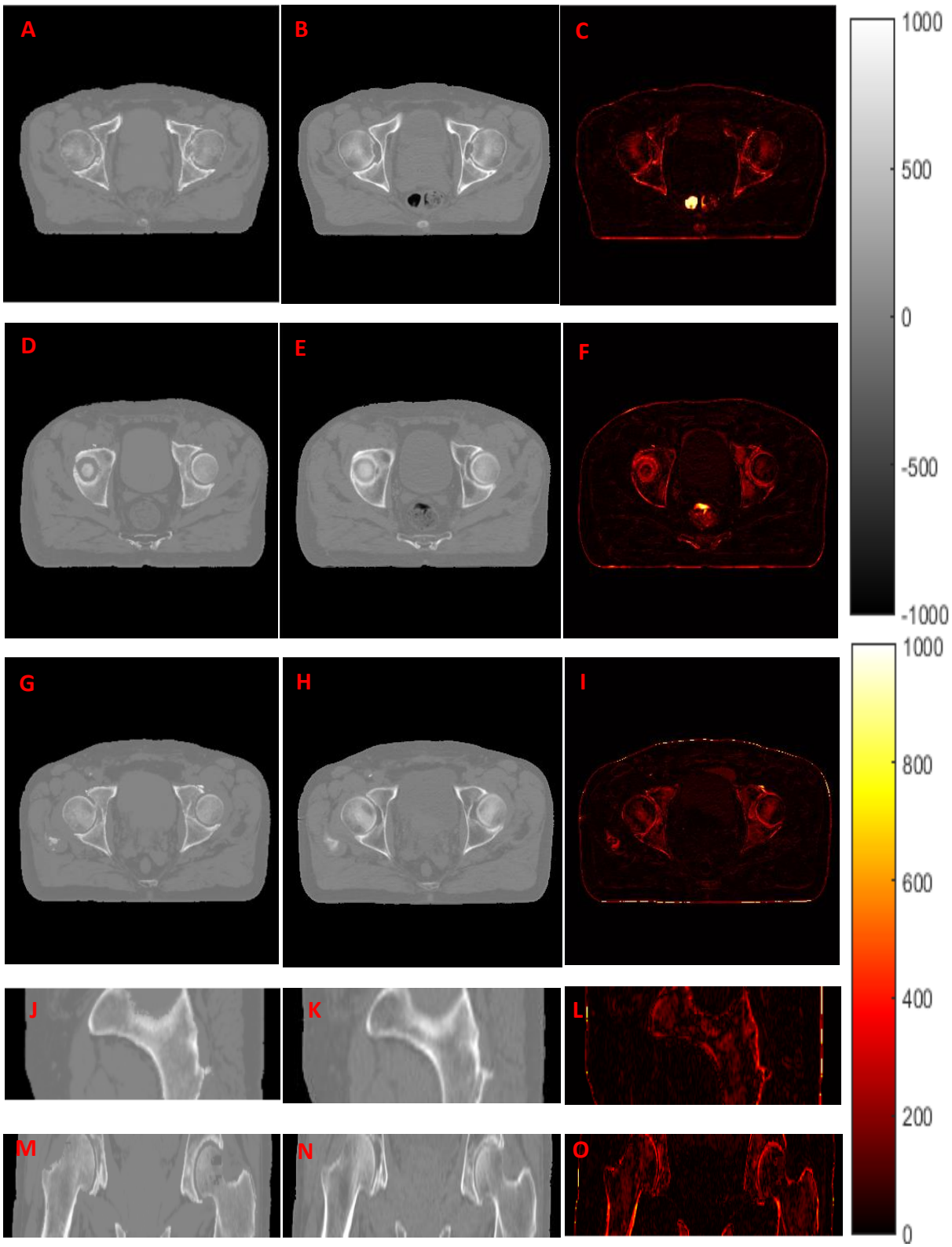

Figure 4.15 – Representation of the obtained pseudo-CTs (first column, figures A, D, G, J, M), the corresponding CT slices (second column, figures B, E, H, K, N) and the absolute difference between the pseudo-CT and CT (third column, figures C, F, I, L, O). The first three rows represent transverse slices for patient 3,5 and 6, respectively. The fourth and fifth rows represent sagittal and coronal slices from patient 5, respectively. The upper scale bar belongs to the pseudo-CT and the real CT whereas the lower belongs to the absolute difference images.

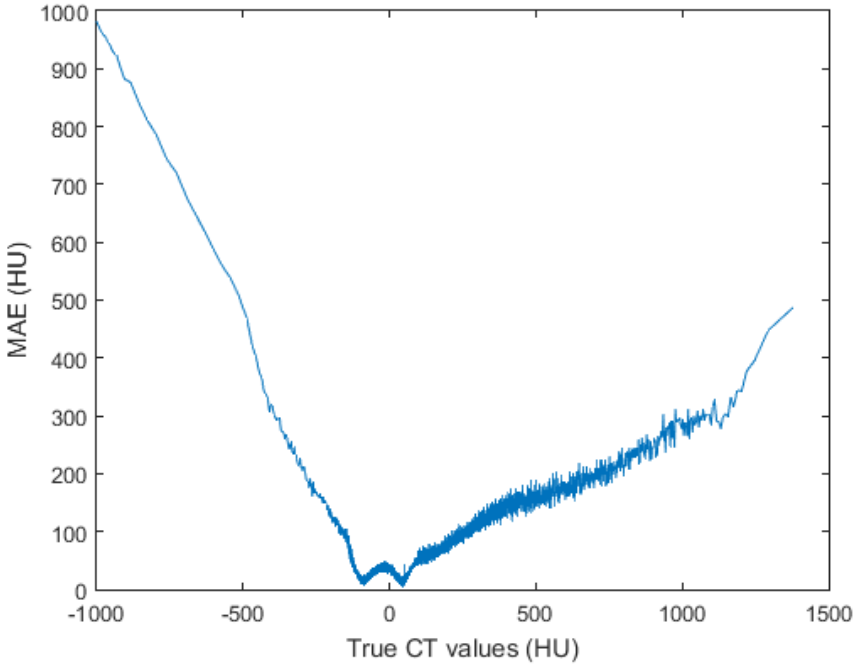

Figure 4.16 – Relation between the MAE and the true CT values, showing that the higher the HU, higher the MAE, excepting for the air (-1000 HU) which was not considered in the soft tissue regression model.

The application of a Gaussian filter as the final step in the pseudo-CT generation workflow had as goal the mitigation of the sharp edges caused by the bone manual segmentation. Furthermore, it can provide a smoother pseudo-CT, especially in the areas where the two intermediate pseudo-CTs touch each other. The effect of the application of the Gaussian filter was analysed by comparing the evaluation metrics before and after applying the Gaussian filter.

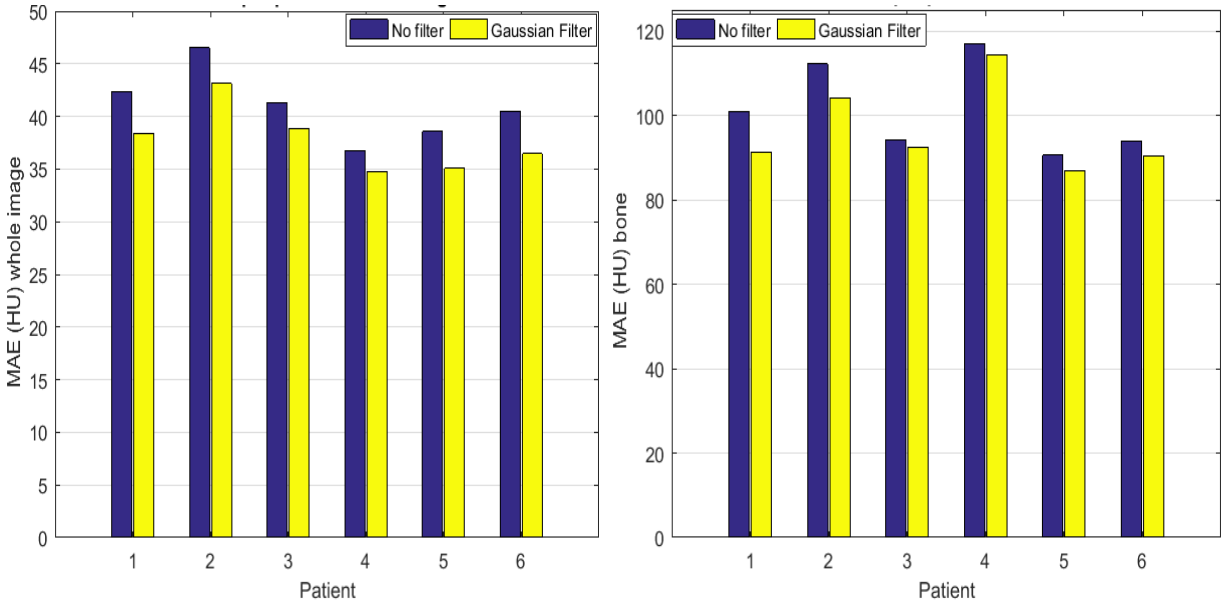

Figure 4.17 – Mean Absolute Error between the pseudo-CT and CT before and after the application of the gaussian filter. **Figure 4.17-A** represents the MAE in the body for all the patients, while **figure 4.17-B** represents the MAE in bone anatomy for all the patients.

Figure 4.17-A represents the MAE in the body of the patient before and after applying the Gaussian filter, while figure 4.17-B represents the MAE in bone anatomy in the same conditions. As it can be seen, the application of the Gaussian filter results in a lower MAE for the whole body of the patient, as well as for the bone anatomy. For the whole-body evaluation, an average MAE of 43.32 ± 4.01 HU was found before the application of the Gaussian filter, while after an average MAE of 37.76 ± 4.01 HU was obtained. Also, an average ME of -2.68 ± 6.32 HU was found after the application of the Gaussian filter, meaning that there is small bias in the pseudo-CT estimation. For bone anatomy, an average MAE of 101.49±10.80 HU was found before the application of the Gaussian filter, while after an average MAE of 96.61±10.49 HU was obtained. The average ME after the application of the Gaussian filter was -10.01±48.04 HU, meaning that the estimation of the HU in bone anatomy is underestimated, mainly due to the presence of cortical bone.

The pseudo-CT was also evaluated using different evaluation metrics as the SSIM and the PSNR. Figure 4.18-A represents the SSIM of the whole body of each patient before and after the application of the Gaussian filter, while figure 4.18-B illustrates the PSNR under the same conditions. As it can be seen in both figures, the application of the Gaussian filter results in higher values of SSIM and PSNR. An average SSIM value of 0.90±0.01 was obtained before the application of the Gaussian filter, while after its application an average SSIM value of 0.91±0.01 was obtained. This fact means that a higher structural resemblance between the pseudo-CT and the respective CT after the application of the Gaussian filter. In the same way, an average PSNR of 23.42±1.43 dB was found before applying the filter, while after a higher average PSNR of 23.92±1.62 dB was obtained. These values of PSNR mean that the reconstruction of the pseudo-CT is less affected by the corrupting errors when the Gaussian filter is applied.

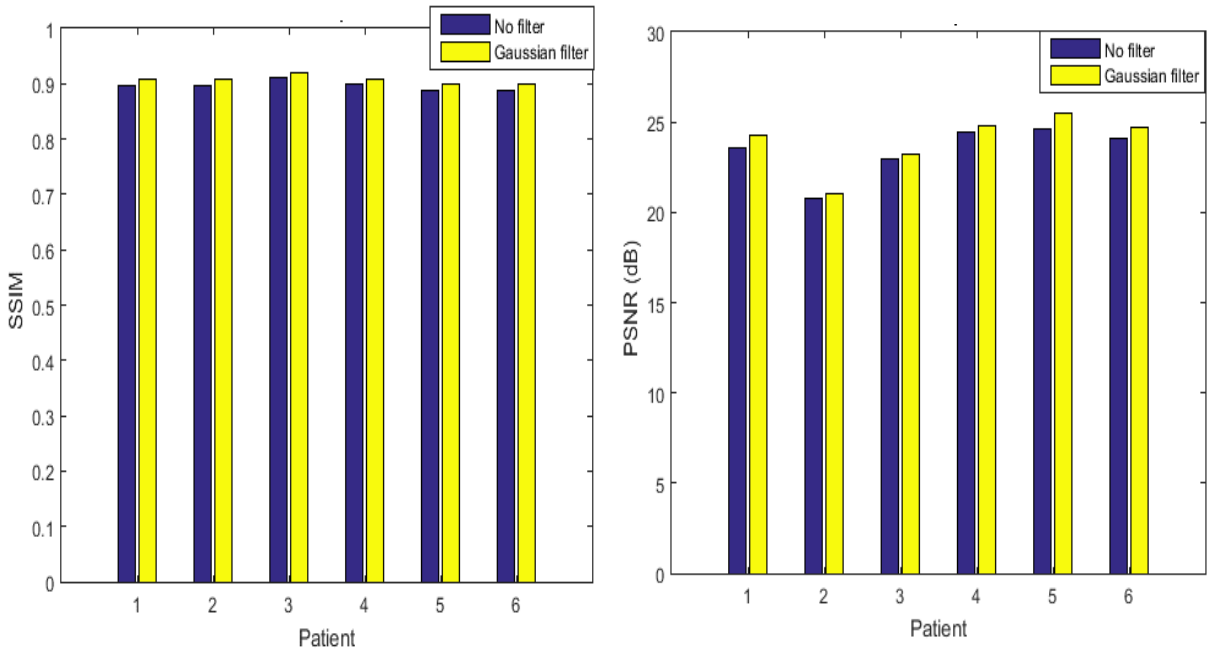

Figure 4.18-A and figure 4.18-B – Representation of the obtained value for each patient of the SSIM and the PSNR, respectively, before and after the application of the gaussian filter

The higher performances in terms of MAE, SSIM and PSNR leads to the conclusion that the application of the Gaussian filter can mitigate the sharp edges caused by the manual segmentation by smoothing the interfaces between different tissue types. In this way, a smoother pseudo-CT is obtained.

Figure 4.19 represents the joint histogram between the true HU values and the predicted HU values. The green line in this histogram represents the ideal case where the predicted HU values are exactly the same as the true HU values. This green line means that the points above this line are overestimated, while the points below this green are underestimated. Also, further the distance of each point to the green line, higher the difference of that value to the true HU value. Analysing this joint histogram, a good correlation between the predicted and true HU values may be found. Also, some of the problems that were already discussed may be visible. It can be seen the presence of underestimation of the higher HU values, corresponding to cortical bone, once the majority of the points in this area in the joint histogram are below the green line. Also, it can be seen that the air in the CT image was classified as soft tissue, as it was already discussed. Furthermore, the effect of misregistrations is here represented by the horizontal deviations from the green line in the area of the soft tissue (-100 HU to 100 HU).

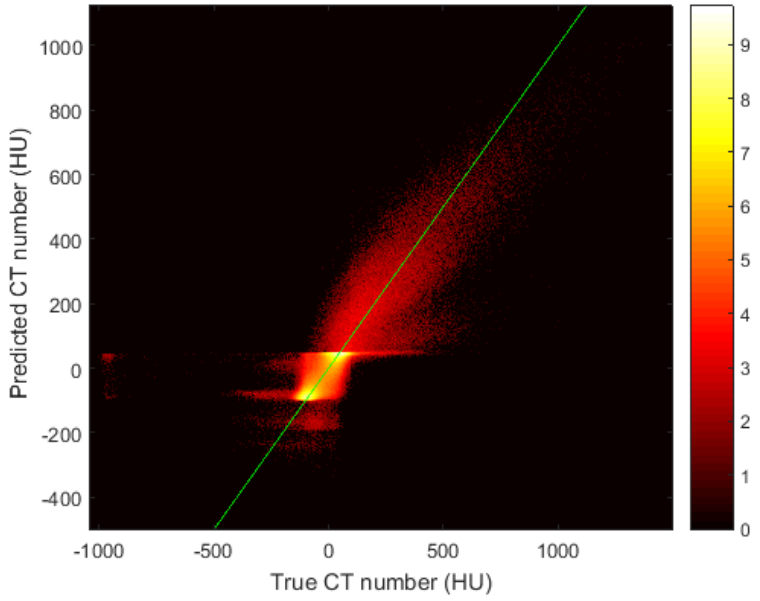

Figure 4.19 – Joint histogram between the true CT number and the predicted CT number. The green line represents the ideal scenario where the pseudo-CT is exactly equal to the real CT. Points below this line indicate a higher HU in the real CT compared to the pseudo-CT, while points above indicate a higher HU in the pseudo-CT compared to the real CT.

The full process of training and validation in the LOOCV had the duration of 6 minutes to perform all the patients, excluding the manual segmentation of the bone. Specifically, the training phase lasted for 5 minutes, while the validation phase only last 1 minute to be performed. The majority of the time required is spent in the bone pseudo-CT generation, once the Gaussian mixture regression is computationally much more expensive than a simple polynomial regression.

Chapter 5

Conclusions and Future Work

MRI is receiving a lot of attention due to its wide range of applications which can bring benefits for techniques such as PET and RTP. However, the lack of correlation between the MR-signal and the attenuation properties of the tissues necessary for calculating the attenuation correction in PET and doses in RTP is a challenge that needs to be overcome to enable PET-MRI and MR-RTP procedures without the use of a CT scan.

In this thesis, a novel pseudo-CT generation method for the pelvic area was developed relying on the exploitation of prior knowledge of the characteristics of the MR signal formation and tissue properties. This method is based on a dual-model regression approach, one for the soft tissues and another one for the bone anatomy based on the water and fat signal and the T_2* decay to construct the pseudo-CT. The input of both models includes the fat fraction image, for the soft tissue regression model, and the fat fraction, water and fat, and R_2* images for the bone regression model. These images were obtained from multi-gradient echo data, whereas the aim of the models was to accurately reproduce the HU estimation as in a traditional CT scan, by constructing pseudo-CT images. Furthermore, it was demonstrated that the inclusion of neighbourhood information, obtained by calculating the standard deviation of each voxel in the 27-neighbourhood, in the regression model for the bone anatomy can significantly improve the estimation of HU values in those areas.

The results obtained in this project present large improvements when compared to other voxel-based methods used for the pelvic area. In this work, an average MAE of 37.76 ± 4.01 HU was obtained. Kim et al. obtained a MAE of 75 HU using several different MR sequences[23], and Korhonen et al. obtained a MAE of 125 HU, by using a T_1/ T_2* weighted MR sequence[70]. This fact proves the superior predicting capability of this approach. Furthermore, it is possible to compare the results with anatomy-based methods. Dowling et al. obtained a MAE of 40.5 HU[66], while Burgos et al. obtained a MAE of 42.9 HU. Burgos et al. also reported a MAE in bone around 100 HU[67]. These results are in the same order in the same order as the ones that were obtained in the method here presented. Thus, it can be concluded that this method allows the generation of a pseudo-CT for the pelvic area with better or identical agreement with the real CT than the methods described in literature. However, the validation in an independent and bigger training and validation group should be performed.

This method presents several advantages over other methods present in literature. First, no registration is needed avoiding the ambiguities caused by registration errors, excepting for the registration errors during the parameter estimation[66] [67]. Moreover, the entire set of features (water, fat, fat fraction and R_2* images) used in this method are obtained through post-processing of a single MR scan, as opposed to multiple scans with different contrasts, which makes it robust against interscan motion and renders the method fast[23]. Furthermore, the computational burden of this method may be reduced in institutions who possess an integrated water-fat decomposition scheme provided by the vendor. In this case, the water-fat decomposition algorithm may be replaced by the water and fat images that are already reconstructed. Thus, the parameter estimation should be performed once per institution and machine in order to overcome possible differences in the hardware and software used.

However, this method also presents some drawbacks. The major limitation of this method is that the bone segmentation is performed manually, increasing the workload and preventing a fully automatic clinical introduction of the method. This drawback is not exclusive of our method, since most voxel-based methods present in literature also rely on manual segmentation[23] [70]. Another limitation of this study is related to the R_2* estimation, which is specific for the echo times used in this project. Although it is expected that the method may be possible to apply with different echo times (requiring the parameter estimation for each set of values used), this hypothesis still needs to be validated. At last, the number of patients used in the training sets is relatively low. By increasing the number of patients in the training set, it is expected to obtain more robust results.

Some improvements to the presented method can be done in order to obtain better results as well as a fully automatic method. First, the acquisition of more data will provide more robust training sets which it is expected to lead to a better HU values estimation.

Also, the inclusion of an automatic MRI bone segmentation method is necessary to turn this method completely automatic and, therefore, can be used in clinical practice without requiring an extra workload for the clinicians. Although, this is still an active area of research, the inclusion of an atlas based segmentation of the bone or the construction of a shape model of the bone are possible solutions to turn this method fully automatic[73] [74]. The resulting method would be a hybrid method, by combining the anatomical information of the bone with the voxelwise conversion of the MR related features into HU values.

Furthermore, the inclusion of other MR features into the bone regression model is possible, allowing a better HU estimation in bone anatomy. Quantitative Susceptibility Mapping (QSM) is a post-processing MR technique which allows the quantification of the susceptibility in different tissues[94] [95]. It is well known that susceptibility values are correlated with the bone mineral density[27]. In this way, another variable may be added to the model. Furthermore, recent advances in QSM techniques allow the quantification of susceptibility values in air and cortical bone even if no signal is available in these areas[96]. As cortical bone and air present different susceptibility values, the segmentation of these tissues may be possible without requiring any anatomic information[97]. Also, it may be possible with the inclusion of this variable that the GMR may be applied to the whole image, allowing the distinction between bone, fat, water and air, and therefore obtain a more accurate pseudo-CT.

At last, it was recently demonstrated that the use of a multi-gradient echo scheme, as well as water-fat reconstructions were useful for the identification of fiducial markers in prostate that are necessary for radiotherapy[98] [99]. In this way, the development of a complete MR-only RTP procedure may be possible only using the features used in this project.

As a final conclusion, we envision that this method may facilitate the development of PET-MRI and MR-only RTP workflows by providing a method to completely replace the use of CT acquisitions, reducing costs associated with its acquisition and sparing the patient to radiation exposure.

References

[1] P. E. Kinahan, B. H. Hasegawa, and T. Beyer, 'X-ray-based attenuation correction for positron emission tomography/computed tomography scanners', *Semin. Nucl. Med.*, vol. 33, no. 3, pp. 166–179, Jul. 2003.

[2] W. Skrzyński, S. Zielińska-Dabrowska, M. Wachowicz, W. Slusarczyk-Kacprzyk, P. F. Kukołowicz, and W. Bulski, 'Computed tomography as a source of electron density information for radiation treatment planning', *Strahlenther. Onkol. Organ Dtsch. Rontgengesellschaft Al*, vol. 186, no. 6, pp. 327–333, Jun. 2010.

[3] E. Teplinsky, A. Pujara, F. J. Esteva, L. Moy, A. Melsaether, and K. L. Jhaveri, 'Detection of metastases in breast cancer: Is whole body PET/MR better than PET/CT?', *J. Clin. Oncol.*, vol. 32, no. 26_suppl, pp. 15–15, Sep. 2014.

[4] A. Afshar-Oromieh *et al.*, 'Comparison of PET/CT and PET/MRI hybrid systems using a 68Ga-labelled PSMA ligand for the diagnosis of recurrent prostate cancer: initial experience', *Eur. J. Nucl. Med. Mol. Imaging*, vol. 41, no. 5, pp. 887–897, May 2014.

[5] M. Souvatzoglou *et al.*, 'Comparison of integrated whole-body [11C]choline PET/MR with PET/CT in patients with prostate cancer', *Eur. J. Nucl. Med. Mol. Imaging*, vol. 40, no. 10, pp. 1486–1499, Oct. 2013.

[6] J. C. Dickson, C. O'Meara, and A. Barnes, 'A comparison of CT- and MR-based attenuation correction in neurological PET', *Eur. J. Nucl. Med. Mol. Imaging*, vol. 41, no. 6, pp. 1176–1189, Jun. 2014.

[7] A. Samarin *et al.*, 'PET/MR imaging of bone lesions--implications for PET quantification from imperfect attenuation correction', *Eur. J. Nucl. Med. Mol. Imaging*, vol. 39, no. 7, pp. 1154–1160, Jul. 2012.

[8] D. Izquierdo-Garcia *et al.*, 'Comparison of MR-based attenuation correction and CT-based attenuation correction of whole-body PET/MR imaging', *Eur. J. Nucl. Med. Mol. Imaging*, vol. 41, no. 8, pp. 1574–1584, Aug. 2014.

[9] S. Hitz *et al.*, 'Systematic Comparison of the Performance of Integrated Whole-Body PET/MR Imaging to Conventional PET/CT for ^{18}F-FDG Brain Imaging in Patients Examined for Suspected Dementia', *J. Nucl. Med. Off. Publ. Soc. Nucl. Med.*, vol. 55, no. 6, pp. 923–931, Jun. 2014.

[10] M. Hofmann, B. Pichler, B. Schölkopf, and T. Beyer, 'Towards quantitative PET/MRI: a review of MR-based attenuation correction techniques', *Eur. J. Nucl. Med. Mol. Imaging*, vol. 36 Suppl 1, pp. S93-104, Mar. 2009.

[11] A. Sciarra *et al.*, 'Advances in magnetic resonance imaging: how they are changing the management of prostate cancer', *Eur. Urol.*, vol. 59, no. 6, pp. 962–977, Jun. 2011.

[12] V. S. Khoo and D. L. Joon, 'New developments in MRI for target volume delineation in radiotherapy', *Br. J. Radiol.*, vol. 79 Spec No 1, pp. S2-15, Sep. 2006.

[13] B. G. Fallone *et al.*, 'First MR images obtained during megavoltage photon irradiation from a prototype integrated linac-MR system', *Med. Phys.*, vol. 36, no. 6, pp. 2084–2088, Jun. 2009.

[14] C. Rasch, R. Steenbakkers, and M. van Herk, 'Target definition in prostate, head, and neck', *Semin. Radiat. Oncol.*, vol. 15, no. 3, pp. 136–145, Jul. 2005.

[15] Prabhakar, 'Comparison of computed tomography and magnetic resonance based target volume in brain tumors'. [Online]. Available: http://www.cancerjournal.net/article.asp?issn=0973-1482;year=2007;volume=3;issue=2;spage=121;epage=123;aulast=Prabhakar. [Accessed: 12-Sep-2017].

[16] A. Fiorentino, R. Caivano, P. Pedicini, and V. Fusco, 'Clinical target volume definition for glioblastoma radiotherapy planning: magnetic resonance imaging and computed tomography', *Clin. Transl. Oncol. Off. Publ. Fed. Span. Oncol. Soc. Natl. Cancer Inst. Mex.*, vol. 15, no. 9, pp. 754–758, Sep. 2013.

[17] K.-H. Su *et al.*, 'Generation of brain pseudo-CTs using an undersampled, single-acquisition UTE-mDixon pulse sequence and unsupervised clustering', *Med. Phys.*, vol. 42, no. 8, pp. 4974–4986, Aug. 2015.

[18] J. M. Edmund and T. Nyholm, 'A review of substitute CT generation for MRI-only radiation therapy', *Radiat. Oncol.*, vol. 12, p. 28, Jan. 2017.

[19] J. E. Holmes and G. M. Bydder, 'MR imaging with ultrashort TE (UTE) pulse sequences: Basic principles', *Radiography*, vol. 11, no. 3, pp. 163–174, Aug. 2005.

[20] T. Nyholm and J. Jonsson, 'Counterpoint: Opportunities and challenges of a magnetic resonance imaging-only radiotherapy work flow', *Semin. Radiat. Oncol.*, vol. 24, no. 3, pp. 175–180, Jul. 2014.

[21] S.-H. Hsu, Y. Cao, K. Huang, M. Feng, and J. M. Balter, 'Investigation of a method for generating synthetic CT models from MRI scans of the head and neck for radiation therapy', *Phys. Med. Biol.*, vol. 58, no. 23, pp. 8419–8435, Dec. 2013.

[22] A. Johansson, M. Karlsson, and T. Nyholm, 'CT substitute derived from MRI sequences with ultrashort echo time', *Med. Phys.*, vol. 38, no. 5, pp. 2708–2714, May 2011.

[23] J. Kim, C. Glide-Hurst, A. Doemer, N. Wen, B. Movsas, and I. J. Chetty, 'Implementation of a novel algorithm for generating synthetic CT images from magnetic resonance imaging data sets for prostate cancer radiation therapy', *Int. J. Radiat. Oncol. Biol. Phys.*, vol. 91, no. 1, pp. 39–47, Jan. 2015.

[24] M. H. Arokoski, J. P. A. Arokoski, P. Vainio, L. H. Niemitukia, H. Kröger, and J. S. Jurvelin, 'Comparison of DXA and MRI methods for interpreting femoral neck bone mineral density', *J. Clin. Densitom. Off. J. Int. Soc. Clin. Densitom.*, vol. 5, no. 3, pp. 289–296, 2002.

[25] V. Keereman, Y. Fierens, T. Broux, Y. De Deene, M. Lonneux, and S. Vandenberghe, 'MRI-based attenuation correction for PET/MRI using ultrashort echo time sequences', *J. Nucl. Med. Off. Publ. Soc. Nucl. Med.*, vol. 51, no. 5, pp. 812–818, May 2010.

[26] J.-P. Kühn *et al.*, 'Proton-density fat fraction and simultaneous R2* estimation as an MRI tool for assessment of osteoporosis', *Eur. Radiol.*, vol. 23, no. 12, pp. 3432–3439, Dec. 2013.

[27] A. V. Dimov, Z. Liu, P. Spincemaille, M. R. Prince, J. Du, and Y. Wang, 'Bone quantitative susceptibility mapping using a chemical species-specific R2* signal model with ultrashort and conventional echo data', *Magn. Reson. Med.*, Mar. 2017.

[28] S. Lee, C. K. Chung, S. H. Oh, and S. B. Park, 'Correlation between Bone Mineral Density Measured by Dual-Energy X-Ray Absorptiometry and Hounsfield Units Measured by Diagnostic CT in Lumbar Spine', *J. Korean Neurosurg. Soc.*, vol. 54, no. 5, pp. 384–389, Nov. 2013.

[29] P. Hoskin and V. Goh, Eds., *Radiotherapy in Practice - Imaging*. Oxford, New York: Oxford University Press, 2010.

[30] J. T. Bushberg, J. A. Seibert, E. M. Leidholdt, and J. M. Boone, *The Essential Physics of Medical Imaging*. Lippincott Williams & Wilkins, 2011.

[31] W. R. Hendee and E. R. Ritenour, *Medical Imaging Physics*. John Wiley & Sons, 2003.

[32] M. Goitein, *Radiation Oncology: A Physicist's-Eye View*. Springer Science & Business Media, 2007.

[33] A. Oppelt, *Imaging Systems for Medical Diagnostics: Fundamentals, Technical Solutions and Applications for Systems Applying Ionizing Radiation, Nuclear Magnetic Resonance and Ultrasound*. John Wiley & Sons, 2011.

[34] U. Schneider, E. Pedroni, and A. Lomax, 'The calibration of CT Hounsfield units for radiotherapy treatment planning', *Phys. Med. Biol.*, vol. 41, no. 1, pp. 111–124, Jan. 1996.
[35] H. Günther, *NMR Spectroscopy: Basic Principles, Concepts and Applications in Chemistry*, 3 edition. Weinheim: Wiley-VCH, 2013.
[36] A. Ribeiro, 'Bone recognition in UTE MR images by artificial neural networks for attenuation correction of brain imaging in MR/PET scanners', MSc, University of Lisbon, Lisbon, 2012.
[37] M. A. Brown and R. C. Semelka, *MRI: Basic Principles and Applications*, 4 edition. Hoboken, N.J: Wiley-Blackwell, 2010.
[38] D. Weishaupt, V. D. Koechli, and B. Marincek, *How does MRI work?: An Introduction to the Physics and Function of Magnetic Resonance Imaging*, 2nd edition. Berlin ; New York: Springer, 2008.
[39] D. W. McRobbie, E. A. Moore, M. J. Graves, and M. R. Prince, *MRI from Picture to Proton*, 2 edition. Cambridge, UK ; New York: Cambridge University Press, 2007.
[40] T. A. Bley, O. Wieben, C. J. François, J. H. Brittain, and S. B. Reeder, 'Fat and water magnetic resonance imaging', *J. Magn. Reson. Imaging JMRI*, vol. 31, no. 1, pp. 4–18, Jan. 2010.
[41] A. Haase, J. Frahm, W. Hänicke, and D. Matthaei, '1H NMR chemical shift selective (CHESS) imaging', *Phys. Med. Biol.*, vol. 30, no. 4, pp. 341–344, Apr. 1985.
[42] G. M. Bydder, J. M. Pennock, R. E. Steiner, S. Khenia, J. A. Payne, and I. R. Young, 'The short TI inversion recovery sequence--an approach to MR imaging of the abdomen', *Magn. Reson. Imaging*, vol. 3, no. 3, pp. 251–254, 1985.
[43] M. Dousset *et al.*, 'Short TI inversion-recovery imaging of the liver: pulse-sequence optimization and comparison with spin-echo imaging', *Radiology*, vol. 171, no. 2, pp. 327–333, May 1989.
[44] J. Ma, 'Dixon techniques for water and fat imaging', *J. Magn. Reson. Imaging JMRI*, vol. 28, no. 3, pp. 543–558, Sep. 2008.
[45] G. Brix, S. Heiland, M. E. Bellemann, T. Koch, and W. J. Lorenz, 'MR imaging of fat-containing tissues: valuation of two quantitative imaging techniques in comparison with localized proton spectroscopy', *Magn. Reson. Imaging*, vol. 11, no. 7, pp. 977–991, 1993.
[46] Q. S. Xiang and L. An, 'Water-fat imaging with direct phase encoding', *J. Magn. Reson. Imaging JMRI*, vol. 7, no. 6, pp. 1002–1015, Dec. 1997.
[47] W. T. Dixon, 'Simple proton spectroscopic imaging', *Radiology*, vol. 153, no. 1, pp. 189–194, Oct. 1984.
[48] G. H. Glover and E. Schneider, 'Three-point Dixon technique for true water/fat decomposition with B0 inhomogeneity correction', *Magn. Reson. Med.*, vol. 18, no. 2, pp. 371–383, Apr. 1991.
[49] D. C. Ghiglia and M. D. Pritt, *Two-Dimensional Phase Unwrapping: Theory, Algorithms, and Software*, 1 edition. New York: Wiley-Interscience, 1998.
[50] S. Moon-Ho Song, S. Napel, N. J. Pelc, and G. H. Glover, 'Phase unwrapping of MR phase images using Poisson equation', *IEEE Trans. Image Process. Publ. IEEE Signal Process. Soc.*, vol. 4, no. 5, pp. 667–676, 1995.
[51] S. B. Reeder *et al.*, 'Iterative decomposition of water and fat with echo asymmetry and least-squares estimation (IDEAL): application with fast spin-echo imaging', *Magn. Reson. Med.*, vol. 54, no. 3, pp. 636–644, Sep. 2005.
[52] H. Yu, S. B. Reeder, A. Shimakawa, J. H. Brittain, and N. J. Pelc, 'Field map estimation with a region growing scheme for iterative 3-point water-fat decomposition', *Magn. Reson. Med.*, vol. 54, no. 4, pp. 1032–1039, Oct. 2005.
[53] H. Yu *et al.*, 'Combination of complex-based and magnitude-based multiecho water-fat separation for accurate quantification of fat-fraction', *Magn. Reson. Med.*, vol. 66, no. 1, pp. 199–206, Jul. 2011.

[54] H. Eggers, B. Brendel, A. Duijndam, and G. Herigault, 'Dual-echo Dixon imaging with flexible choice of echo times', *Magn. Reson. Med.*, vol. 65, no. 1, pp. 96–107, Jan. 2011.
[55] J. Berglund, 'Separation of Water and Fat Signal in Magnetic Resonance Imaging: Advances in Methods Based on Chemical Shift', PhD, Uppsala University, Uppsala, 2011.
[56] D. Hernando, P. Kellman, J. P. Haldar, and Z.-P. Liang, 'Robust water/fat separation in the presence of large field inhomogeneities using a graph cut algorithm', *Magn. Reson. Med.*, vol. 63, no. 1, pp. 79–90, Jan. 2010.
[57] H. Yu, A. Shimakawa, C. A. McKenzie, E. Brodsky, J. H. Brittain, and S. B. Reeder, 'Multi-Echo Water-Fat Separation and Simultaneous R2* Estimation with Multi-Frequency Fat Spectrum Modeling', *Magn. Reson. Med. Off. J. Soc. Magn. Reson. Med. Soc. Magn. Reson. Med.*, vol. 60, no. 5, pp. 1122–1134, Nov. 2008.
[58] H. Yu *et al.*, 'Multiecho reconstruction for simultaneous water-fat decomposition and T2* estimation', *J. Magn. Reson. Imaging JMRI*, vol. 26, no. 4, pp. 1153–1161, Oct. 2007.
[59] D. Hernando, J. P. Haldar, B. P. Sutton, J. Ma, P. Kellman, and Z.-P. Liang, 'Joint Estimation of Water/Fat Images and Field Inhomogeneity Map', *Magn. Reson. Med. Off. J. Soc. Magn. Reson. Med. Soc. Magn. Reson. Med.*, vol. 59, no. 3, pp. 571–580, Mar. 2008.
[60] R. Merris, *Graph Theory*, 1 edition. New York: Wiley-Interscience, 2000.
[61] V. Kolmogorov and R. Zabin, 'What energy functions can be minimized via graph cuts?', *IEEE Trans. Pattern Anal. Mach. Intell.*, vol. 26, no. 2, pp. 147–159, Feb. 2004.
[62] R. B. Buxton, G. L. Wismer, T. J. Brady, and B. R. Rosen, 'Quantitative proton chemical-shift imaging', *Magn. Reson. Med.*, vol. 3, no. 6, pp. 881–900, Dec. 1986.
[63] C.-Y. Liu, C. A. McKenzie, H. Yu, J. H. Brittain, and S. B. Reeder, 'Fat quantification with IDEAL gradient echo imaging: correction of bias from T(1) and noise', *Magn. Reson. Med.*, vol. 58, no. 2, pp. 354–364, Aug. 2007.
[64] J. Uh, T. E. Merchant, Y. Li, X. Li, and C. Hua, 'MRI-based treatment planning with pseudo CT generated through atlas registration', *Med. Phys.*, vol. 41, no. 5, p. 051711, May 2014.
[65] J. Sjölund, D. Forsberg, M. Andersson, and H. Knutsson, 'Generating patient specific pseudo-CT of the head from MR using atlas-based regression', *Phys. Med. Biol.*, vol. 60, no. 2, p. 825, 2015.
[66] J. A. Dowling *et al.*, 'An atlas-based electron density mapping method for magnetic resonance imaging (MRI)-alone treatment planning and adaptive MRI-based prostate radiation therapy', *Int. J. Radiat. Oncol. Biol. Phys.*, vol. 83, no. 1, pp. e5-11, May 2012.
[67] N. Burgos *et al.*, 'Iterative framework for the joint segmentation and CT synthesis of MR images: application to MRI-only radiotherapy treatment planning', *Phys. Med. Biol.*, vol. 62, no. 11, p. 4237, 2017.
[68] A. L. Chin, A. Lin, S. Anamalayil, and B.-K. K. Teo, 'Feasibility and limitations of bulk density assignment in MRI for head and neck IMRT treatment planning', *J. Appl. Clin. Med. Phys.*, vol. 15, no. 5, p. 4851, Sep. 2014.
[69] M. E. Korsholm, L. W. Waring, and J. M. Edmund, 'A criterion for the reliable use of MRI-only radiotherapy', *Radiat. Oncol. Lond. Engl.*, vol. 9, p. 16, Jan. 2014.
[70] J. Korhonen, M. Kapanen, J. Keyriläinen, T. Seppälä, and M. Tenhunen, 'A dual model HU conversion from MRI intensity values within and outside of bone segment for MRI-based radiotherapy treatment planning of prostate cancer', *Med. Phys.*, vol. 41, no. 1, p. 011704, Jan. 2014.
[71] M. Kapanen and M. Tenhunen, 'T1/T2*-weighted MRI provides clinically relevant pseudo-CT density data for the pelvic bones in MRI-only based radiotherapy treatment planning', *Acta Oncol. Stockh. Swed.*, vol. 52, no. 3, pp. 612–618, Apr. 2013.

[72] D. Andreasen, K. Van Leemput, R. H. Hansen, J. A. L. Andersen, and J. M. Edmund, 'Patch-based generation of a pseudo CT from conventional MRI sequences for MRI-only radiotherapy of the brain', *Med. Phys.*, vol. 42, no. 4, pp. 1596–1605, Apr. 2015.
[73] H. Arabi and H. Zaidi, 'Comparison of atlas-based techniques for whole-body bone segmentation', *Med. Image Anal.*, vol. 36, pp. 98–112, Feb. 2017.
[74] J. Schmid, J. Kim, and N. Magnenat-Thalmann, 'Robust statistical shape models for MRI bone segmentation in presence of small field of view', *Med. Image Anal.*, vol. 15, no. 1, pp. 155–168, Feb. 2011.
[75] D. A. Cohn, *Active Learning with Statistical Models*. PN, 1995.
[76] N. Laird, '14 The EM algorithm', in *Handbook of Statistics*, vol. 9, Supplement C vols, Elsevier, 1993, pp. 509–520.
[77] A. K. Jain, 'Data clustering: 50 years beyond K-means', *Pattern Recognit. Lett.*, vol. 31, no. 8, pp. 651–666, Jun. 2010.
[78] D. Andreasen, 'Creating a Pseudo-CT from MRI fror MRI-only based Radiation Therapy Planning', MSc, Technical University of Denmark, 2013.
[79] V. Cherkassky and Y. Ma, 'Comparison of model selection for regression', *Neural Comput.*, vol. 15, no. 7, pp. 1691–1714, Jul. 2003.
[80] S. Klein, M. Staring, K. Murphy, M. A. Viergever, and J. P. W. Pluim, 'elastix: a toolbox for intensity-based medical image registration', *IEEE Trans. Med. Imaging*, vol. 29, no. 1, pp. 196–205, Jan. 2010.
[81] W. D. Penny, K. J. Friston, J. T. Ashburner, S. J. Kiebel, and T. E. Nichols, *Statistical Parametric Mapping: The Analysis of Functional Brain Images*. Academic Press, 2011.
[82] A. Sotiras, C. Davatzikos, and N. Paragios, 'Deformable Medical Image Registration: A Survey', *IEEE Trans. Med. Imaging*, vol. 32, no. 7, pp. 1153–1190, Jul. 2013.
[83] M. Staring, S. Klein, and J. P. W. Pluim, 'A rigidity penalty term for nonrigid registration', *Med. Phys.*, vol. 34, no. 11, pp. 4098–4108, Nov. 2007.
[84] A. K. Jain, *Fundamentals of Digital Image Processing*, 1 edition. Englewood Cliffs, NJ: Pearson, 1988.
[85] H. H. Hu *et al.*, 'ISMRM Workshop on Fat–Water Separation: Insights, Applications and Progress in MRI', *Magn. Reson. Med. Off. J. Soc. Magn. Reson. Med. Soc. Magn. Reson. Med.*, vol. 68, no. 2, pp. 378–388, Aug. 2012.
[86] G. H. Glover, 'Multipoint Dixon technique for water and fat proton and susceptibility imaging', *J. Magn. Reson. Imaging JMRI*, vol. 1, no. 5, pp. 521–530, Oct. 1991.
[87] S. B. Reeder *et al.*, 'Water-fat separation with IDEAL gradient-echo imaging', *J. Magn. Reson. Imaging JMRI*, vol. 25, no. 3, pp. 644–652, Mar. 2007.
[88] D. Hernando *et al.*, 'R2* estimation using "in-phase" echoes in the presence of fat: the effects of complex spectrum of fat', *J. Magn. Reson. Imaging JMRI*, vol. 37, no. 3, pp. 717–726, Mar. 2013.
[89] N. Otsu, 'A Threshold Selection Method from Gray-Level Histograms', *IEEE Trans. Syst. Man Cybern.*, vol. 9, no. 1, pp. 62–66, Jan. 1979.
[90] K. H. Zou *et al.*, 'Statistical Validation of Image Segmentation Quality Based on a Spatial Overlap Index', *Acad. Radiol.*, vol. 11, no. 2, pp. 178–189, Feb. 2004.
[91] A. P. Zijdenbos, B. M. Dawant, R. A. Margolin, and A. C. Palmer, 'Morphometric analysis of white matter lesions in MR images: method and validation', *IEEE Trans. Med. Imaging*, vol. 13, no. 4, pp. 716–724, 1994.
[92] S. Calinon, *Robot Programming by Demonstration: A Probabilistic Approach*. CRC, 2009.
[93] M. Nixon, *Feature Extraction & Image Processing*. Academic Press, 2008.

[94] Y. Wang and T. Liu, ‘Quantitative susceptibility mapping (QSM): Decoding MRI data for a tissue magnetic biomarker’, *Magn. Reson. Med.*, vol. 73, no. 1, pp. 82–101, Jan. 2015.
[95] J. R. Reichenbach, F. Schweser, B. Serres, and A. Deistung, ‘Quantitative Susceptibility Mapping: Concepts and Applications’, *Clin. Neuroradiol.*, vol. 25 Suppl 2, pp. 225–230, Oct. 2015.
[96] Z. Liu, Y. Kee, D. Zhou, Y. Wang, and P. Spincemaille, ‘Preconditioned total field inversion (TFI) method for quantitative susceptibility mapping’, *Magn. Reson. Med.*, vol. 78, no. 1, pp. 303–315, Jul. 2017.
[97] S. Buch, S. Liu, Y. Ye, Y.-C. N. Cheng, J. Neelavalli, and E. M. Haacke, ‘Susceptibility mapping of air, bone, and calcium in the head’, *Magn. Reson. Med.*, vol. 73, no. 6, pp. 2185–2194, Jun. 2015.
[98] M. Kapanen, J. Collan, A. Beule, T. Seppälä, K. Saarilahti, and M. Tenhunen, ‘Commissioning of MRI-only based treatment planning procedure for external beam radiotherapy of prostate’, *Magn. Reson. Med.*, vol. 70, no. 1, pp. 127–135, Jul. 2013.
[99] M. Maspero *et al.*, ‘Evaluation of an automatic MR-based gold fiducial marker localisation method for MR-only prostate radiotherapy’, *Phys. Med. Biol.*, Aug. 2017.

Appendix

Appendix I

This appendix presents the MATLAB list of input parameters for the water-fat decomposition algorithm used in this project.

```
algoParams.species(1).name = 'water';
algoParams.species(1).frequency = 0;
algoParams.species(1).relAmps = 1;
algoParams.species(2).name = 'fat';
algoParams.species(2).frequency = [-3.80, -3.40, -2.60, -1.94, -
0.39, 0.60];
algoParams.species(2).relAmps = [0.087 0.693 0.128 0.004 0.039
0.048];

algoParams.size_clique = 1; algoParams.range_r2star = [0 0]; % Range
of R2* values
algoParams.NUM_R2STARS = 1; % Number of R2* values for quantization
algoParams.range_fm = [-700 700]; % Range of field map values
algoParams.NUM_FMS = 301; % Number of field map values to discretize
algoParams.NUM_ITERS = 40; % Number of graph cut iterations
algoParams.SUBSAMPLE =4; % Spatial subsampling for field map
estimation (for speed)
algoParams.DO_OT = 0; % 0,1 flag to enable optimization transfer
descent (final stage of field map estimation)
algoParams.LMAP_POWER = 2; % Spatially-varying regularization (2
gives ~ uniformn resolution)
algoParams.lambda = 0.05; % Regularization parameter
algoParams.LMAP_EXTRA = 0.02; % More smoothing for low-signal
regions
algoParams.TRY_PERIODIC_RESIDUAL = 0;
```